nature chemical biology

Article

https://doi.org/10.1038/s41589-024-01572-x

DNA-functionalized artificial mechanoreceptor for de novo force-responsive signaling

Received: 15 February 2023

Accepted: 7 February 2024

Published online: 6 March 2024

Check for updates

Sihui Yang[1], Miao Wang[1], Dawei Tian[2,3], Xiaoyu Zhang[2,3], Kaiqing Cui[1], Shouqin Lü[2,3], Hong-hui Wang[1], Mian Long[2,3] & Zhou Nie[1]

Synthetic signaling receptors enable programmable cellular responses coupling with customized inputs. However, engineering a designer force-sensing receptor to rewire mechanotransduction remains largely unexplored. Herein, we introduce nongenetically engineered artificial mechanoreceptors (AMRs) capable of reprogramming non-mechanoresponsive receptor tyrosine kinases (RTKs) to sense user-defined force cues, enabling de novo-designed mechanotransduction. AMR is a modular DNA–protein chimera comprising a mechanosensing-and-transmitting DNA nanodevice grafted on natural RTKs via aptameric anchors. AMR senses intercellular tensile force via an allosteric DNA mechano-switch with tunable piconewton-sensitive force tolerance, actuating a force-triggered dynamic DNA assembly to manipulate RTK dimerization and activate intracellular signaling. By swapping the force-reception ligands, we demonstrate the AMR-mediated activation of c-Met, a representative RTK, in response to the cellular tensile forces mediated by cell-adhesion proteins (integrin, E-cadherin) or membrane protein endocytosis (CI-M6PR). Moreover, AMR also allows the reprogramming of FGFR1, another RTK, to customize mechanobiological function, for example, adhesion-mediated neural stem cell maintenance.

Cells constantly sense environmental cues and respond with distinct cellular behaviors via receptor-mediated signaling. Synthetic receptor engineering has been considerably exploited to endow receptors with programmable responsiveness to diverse user-defined inputs, such as small molecules, soluble or membrane-bound ligands and light[1–3]. Rationally rewiring the sense-and-respond program of cellular receptors enables controllable cellular functions, which are increasingly used for biological research and therapeutic applications[4]. Among diverse signal inputs, mechanical force is a crucial physical cue in cell communications, essential for homeostasis, development and pathogenesis[5,6]. However, despite the vital role of mechanobiology, it remains challenging to engineer synthetic receptors to customize cellular signaling with mechanical force-responsive properties.

On sensing force-based inputs from the extracellular matrix (ECM) or neighboring cells, natural mechanoreceptors (that is, integrins, cadherins, T cell antigen receptor and Notch) implement force-induced conformational change and trigger mechanotransduction to regulate cellular responses[7,8]. Recently, a few synthetic

[1]State Key Laboratory of Chemo/Biosensing and Chemometrics, Hunan Provincial Key Laboratory of Biomacromolecular Chemical Biology, College of Chemistry and Chemical Engineering, College of Biology, Hunan University, Changsha, China. [2]Center of Biomechanics and Bioengineering, Key Laboratory of Microgravity (National Microgravity Laboratory), Beijing Key Laboratory of Engineered Construction and Mechanobiology, Institute of Mechanics, Chinese Academy of Sciences, Beijing, China. [3]School of Engineering Science, University of Chinese Academy of Sciences, Beijing, China. e-mail: niezhou.hnu@gmail.com

https://doi.org/10.1038/s41589-024-01572-x

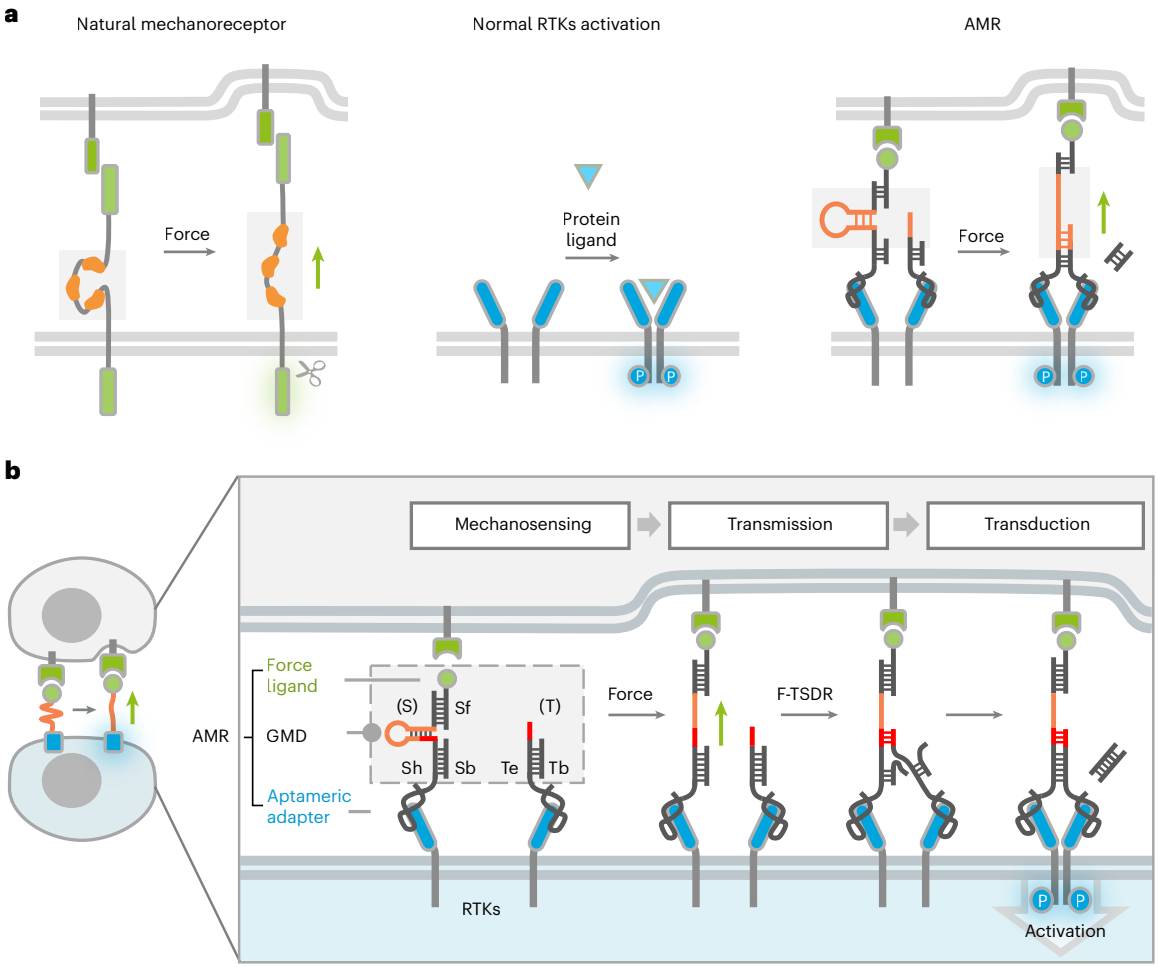

Fig. 1 | Schematic illustration of the AMR. a, The conceptual design of AMR for reprograming non-mechanoresponsive RTKs with force responsiveness. **b**, Working model of AMR implementation. The GMD nanodevices are nongenetically functionalized on natural cell-surface RTKs to constitute the AMRs, which enables the cells to sense the neighbor cell-sending tensile force via an allosteric switch of the DNA hairpin motif, thereby implementing F-TSDR to promote RTK dimerization and intracellular downstream signaling.

mechanoreceptors, including synthetic Notch receptors (synNotch) and synthetic cell-adhesion molecules (synCAMs), have been genetically engineered from their cognate natural mechano-switch scaffolds to customize input force-output signaling programs for tissue patterning or immunotherapy[9,10]. However, generalized mechanoreceptor engineering approaches are still hampered by the limited repertoire of natural mechano-switch scaffolds, the incomplete understanding of natural mechanosensing mechanisms and the inability to reprogram a broader range of non-mechanoresponsive receptors with customized mechanosensing capabilities. Therefore, it is highly desirable to develop a de novo mechanoreceptor design strategy independent of natural mechanosensory mechanisms.

Herein, we present a de novo design of an artificial mechanoreceptor (AMR) to reprogram the non-mechanoresponsive cell-surface receptors to sense user-defined intercellular tensile force (Fig. 1). AMR is a highly modular DNA–protein chimeric platform comprising a generalized mechanosensing-and-transmitting DNA (GMD) nanodevice that functions as a plug-and-play molecular adapter to nongenetically engineer a natural cell-surface receptor for force-induced signaling. In the working model of AMR, the GMD device senses the neighbor cell-sending tensile force via an allosteric DNA switch, implementing a force-triggered dynamic DNA nanoassembly to promote receptor dimerization and intracellular signaling of the force-receiving cells. The generalizability of AMR enables flexible customization of the inputting force-reception ligands to sense diverse cell-generated tensile forces mediated by cell-adhesion molecules (integrin, E-cadherin) or membrane protein endocytosis (CI-M6PR). The signaling output of AMR is also versatile in regulating distinct non-mechanoresponsive cell-surface receptors (c-Met or FGFR1). This AMR-rewired input–output program achieves the de novo-designed mechanotransduction to reprogram mechanobiological function, for example, adhesion-mediated neural stem cell (NSC) maintenance. The DNA-functionalized AMR presents alternative mechanotransduction machinery independent of natural protein-based mechano-switches. The capability of AMR to repurpose a non-mechanoresponsive receptor to transmit force-induced signaling would provide a promising synthetic toolkit for mechanobiological research and biomedical applications.

Results

Design and implementation of the AMR platform

Inspired by the force-induced deformation in natural mechanoreceptor activation, we couple a DNA mechanosensing allosteric switch with a deformation-triggered DNA dynamic reaction in AMR, creating a new interplay between mechanical forces and endogenous receptor signaling via dynamic DNA nanotechnology[11–13] (Fig. 1a). As a proof-of-concept, we use AMR to manipulate RTKs, a pivotal receptor family regulating morphogenesis, migration and proliferation[14]. Typically, RTKs are activated by target-induced dimerization, and their native targets are polypeptide ligands, for example, growth factors[15]. Although there were engineered RTKs that enabled cells to sense user-specified molecules

https://doi.org/10.1038/s41589-024-01572-x

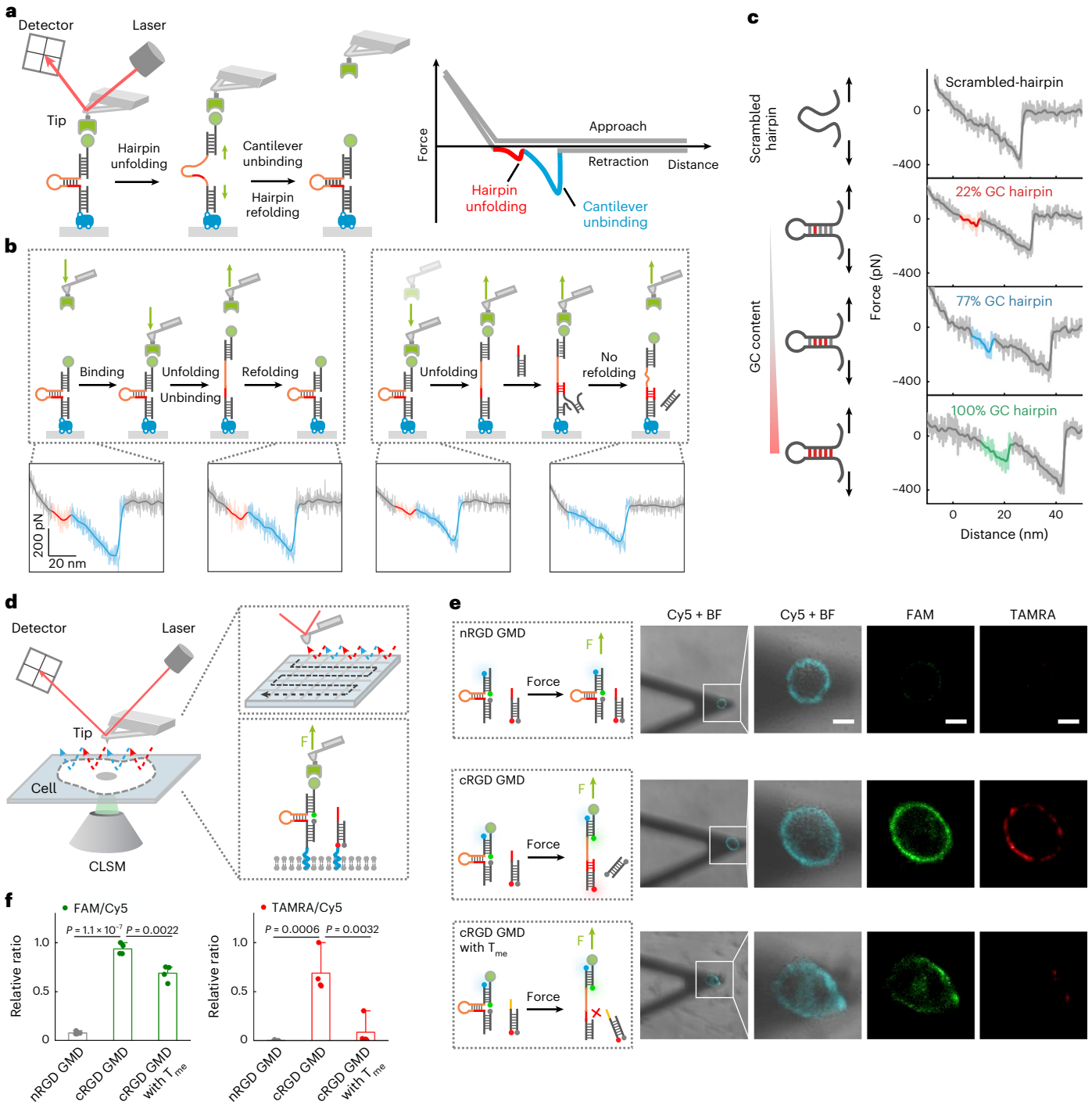

Fig. 2 | Implementation of GMD under external tractile force. a, The schematic of the experimental setting to probe the hairpin unfolding and refolding performance of cRGD-S under the tractile force loaded by AFM (left). In a single-molecular pulling experiment, the cantilever tip first approached the surface (at 300 nm s^{-1}) and contacted for 20 ms, followed by the retraction of the cantilever (at 300 nm s^{-1}). A typical FE curve shows a small peak of hairpin unfolding followed by a sharp rupture peak of cRGD-integrin unbinding (right). **b**, Representative FE curves of multiple AFM-pulling experiments between the integrin-functionalized cantilever tip and cRGD-S-modified surface with or without soluble T modules. **c**, The representative FE curves to compare the performance of cRGD-S containing hairpins with varying GC contents. **d**, Characterization of the performance of GMD on cell membranes under AFM-loaded tractile force combined with CLSM. **e**, Representative images visualizing the hairpin unfolding and sequential F-TSDR events on the cell membrane of HeLa cells engineered with nRGD GMD, cRGD GMD and cRGD GMD with T_{me} (T module with mutated engaging sequence), respectively. Cy5, FAM and TAMRA channels were shown in blue, green and red, respectively. Scale bars, 10 μm. **f**, Quantification of the relative FAM/Cy5 and TAMRA/Cy5 ratio as shown in **e** ($n = 4$). Data represent mean ± s.d. from independent experiments, and significance was determined by unpaired two-tailed Student's *t*-test.

or light[3], an approach to engineer RTKs with mechanoresponsiveness remains absent. Hence, we have devised GMD nanodevices to reprogram RTKs into intercellular force-responsive AMRs.

A GMD nanodevice consists of two adaptable modules, a sensor (S) and a transmitter (T), hooking on the extracellular region of the RTK via the extended specific aptameric anchor to constitute

two DNA-based heterogenous AMR monomers (Fig. 1b and Supplementary Fig. 1). S module is the self-assembly comprising three DNA strands: a strand containing a folded stem-loop hairpin with two flanking arms (Sh) that hybridize with a strand displaying a force-reception ligand (Sf) and a blocking strand (Sb), respectively. T module is a DNA duplex (Te–Tb) with a 5′ overhang single-stranded engaging region ready for DNA strand displacement reaction. The mechanosensation of GMD is dependent on two key functional motifs: the swappable force-receiving ligand displayed on Sf and the hairpin motif on Sh as a digital mechano-switch to measure tensile force and elicit a conformation transition. The force transmission of GMD relies on a unique force-triggered toehold-mediated strand displacement reaction (F-TSDR) between S and T modules. Without force loading, the toehold domain in Sh is sequestered in the hairpin stem and is inaccessible to Te. On tractile forces transmitted by the ligand on Sf, the hairpin motif of Sh mechanically unfolds and unmasks the toehold domain to bind to the engaging region on the T module, initiating cascaded strand displacement for force transmission. The F-TSDR leads to the dissociation of the blocking strands (Sb and Tb) and the hybridization of two receptor-hooking strands (Sh and Te). Consequently, two anchored RTK monomers are dimerized to trigger autophosphorylation and for signal activation, presenting the mechano-transducing output of AMR. Therefore, the AMR strategy represents a bottom-up approach to repurpose non-mechanoresponsive RTKs for a force-induced cellular response.

The performance of GMD under external tractile forces

Given its critical role in the mechano-transmission of AMR, the force-responsive performance of GMD was first examined by atomic force microscopy (AFM) based on single-molecule force spectroscopy[16] (Fig. 2a). Here, the S module was conjugated with a cyclic Arg-Gly-Asp-D-Phe-Lys (cRGDfk) ligand (cRGD-S) via thiol-maleimide chemistry and immobilized on the substrate surface by biotin–streptavidin interaction (Supplementary Fig. 2 and Supplementary Table 1). The AFM cantilever tip was functionalized with recombinant integrin αvβ3 protein to interact with cRGD-S, mimicking the integrin-mediated cellular forces[17] (Fig. 2a). In a single-molecular pulling experiment, the cantilever tip first approached the surface and contacted, followed by the retraction of the cantilever. A typical force-extension (FE) curve showed that the stretching of cRGD-S exhibited a small peak followed by a sharp rupture peak of cRGD-integrin dissociation (Fig. 2b). The small peak in the FE curve represents the mechanical fingerprint of the hairpin unfolding of the cRGD-S module, as confirmed by its abolishment in the hairpin-absent control (cRGD-S_h) (Extended Data Fig. 1). Furthermore, increasing the hairpin stability by elevating the guanine-cytosine (GC) contents gradually increased the force magnitude of the unfolding peak and their cognate persistence lengths were consistent with the predicted unfolding free energies according to the worm-like chain model analysis[18,19] (Fig. 2c and Extended Data Fig. 2). The unfolded cRGD-S refolded after one round of measurement, showing its specific unfolding peak again in the second round of measurement (Fig. 2b).

To confirm that F-TSDR is force-triggered as designed, we stretched cRGD-S in the presence of the soluble T module. The small hairpin-unfolding peak in the FE curve disappeared in the second round of measurement, accordant with that of the Sf–Sh–Te triplex, the expected product of F-TSDR, which prevents the unfolded hairpin from refolding (Extended Data Fig. 3). In comparison, the T module with mutated engaging sequence (T_{me}) restored the hairpin-unfolding peak, verifying the role of F-TSDR in force transmission (Extended Data Fig. 3). The idealized free energy landscape shows that force-induced hairpin unfolding significantly overcomes the hidden-toehold-caused activation energy barrier to energetically and kinetically facilitate the reactions[20,21] (Supplementary Figs. 3 and 4). These results indicate that GMD can sense external tractile forces to promote F-TSDR for force transmission.

Next, we evaluated the performance of GMD on cell membranes under the FE curve-based AFM combined with confocal laser scanning microscopy (CLSM) (Fig. 2d). The cRGD-S and T (together as cRGD GMD) were displayed on the membrane of HeLa cells via cholesterol anchors[22], and the cRGD-S was Cy5-tagged for labeling GMD-functionalized cells (Supplementary Table 2). To monitor the hairpin unfolding and sequential F-TSDR, we labeled cRGD-S and T with two fluorophore-quencher paired reporters, FAM-BHQ1 and TAMRA-BHQ2, respectively (Supplementary Fig. 5). The integrin-functionalized cantilever tip was raster-scanned across the cell membrane to exert tractile forces at discrete points (Fig. 2d and Supplementary Fig. 6). Once the force exceeds the threshold, the hairpin of cRGD-S unfolds, which separates the FAM-BHQ1 pair to generate FAM fluorescence as a force-sensing readout. Subsequently, the unmasked toehold of cRGD-S interacts with T to dissociate the BHQ2 and generate TAMRA fluorescence, reporting F-TSDR event for force transmission (Supplementary Fig. 4). With continuous contact, the performance of numerous GMDs can be monitored in situ by the dual-color readout under CLSM. The results showed that the GMD-functionalized cell under cantilever-loaded tractile forces simultaneously displayed strong fluorescence at both FAM and TAMRA channels, whereas both signals were absent in the control without cRGD ligand (nRGD GMD) (Fig. 2e,f). Moreover, the T_{me} module decreased the TAMRA signal and slightly affected the FAM signal, verifying the essential role of F-TSDR in force transmission. Together, we validate that GMD can sense and transmit the external tractile forces via F-TSDR on the cell membrane.

Characterization of GMD in sense-and-transmit force input

We next explored the validity of GMD under integrin-mediated forces generated in cell adhesion (Fig. 3a). NIH3T3 cell, an integrin-positive cell line, was spread on the cRGD-S-modified glass substrate. Total internal reflection fluorescence microscopy (TIRFM) was used to monitor cell-adhesion force-induced cRGD-S hairpin deformation by its Cy3-BHQ1 reporter and subsequent F-TSDR process with excess soluble T containing Alexa 647-BHQ2 reporter (Fig. 3b and Supplementary Figs. 7–9). Specifically, cRGD-S tailored with a hairpin motif containing 22% GC content with the predetermined force tolerance of 4.5 pN (ref. 18), an appropriate threshold to measure integrin-mediated physiologic forces (Supplementary Table 1). Within 30 min, NIH3T3 cells fully spread on the cRGD-S-modified surfaces with visible lamellipodia, and both Cy3 and Alexa 647 signals were bright and colocalized at the cell-substrate contact zone, reporting the force-sensing and transmitting events (Fig. 3b). As expected, free T_{me} induced negligible effect on cell spreading as well as Cy3 signal but failed to generate Alexa 647 signal due to lack of F-TSDR (Fig. 3b). Without the cRGD ligand, cells displayed minimal spreading without force-sensing and transmitting signals, confirming their dependency on the integrin–cRGD interaction-mediated cell adhesion (Fig. 3b). Similarly, treatment by Blebbistatin, an inhibitor of myosin II ATPase[23], inhibited cell spreading and diminished both signals, suggesting that the force activating GMD is derived from actomyosin activity (Fig. 3b).

In multicellular environments, junctional complexes function as physical bridges transmitting intercellular forces to tightly regulate cell–cell communication[24]. We next evaluated the performance of GMD in responding to intercellular forces by displaying cRGD GMD on NIH3T3 cells via cholesterol anchors (Fig. 3c and Supplementary Table 2). The membrane-anchored cRGD GMD complexed with the integrin of neighboring cells, reconstituting artificial cell–cell junctions (Fig. 3c). Sh was tagged with Cy5 to normalize cRGD GMD distribution on the cell membrane (Supplementary Table 2). Combining with FAM-BHQ1 and TAMRA-BHQ2, the force-sensing and force-transmitting events of cRGD GMD were ratiometrically mapped by monitoring the reporter-to-reference ratios of FAM/Cy5 and TAMRA/Cy5, respectively. As a result, we observed that the FAM/Cy5 and TAMRA/Cy5 signals simultaneously increased in cRGD GMD-functionalized cells

https://doi.org/10.1038/s41589-024-01572-x

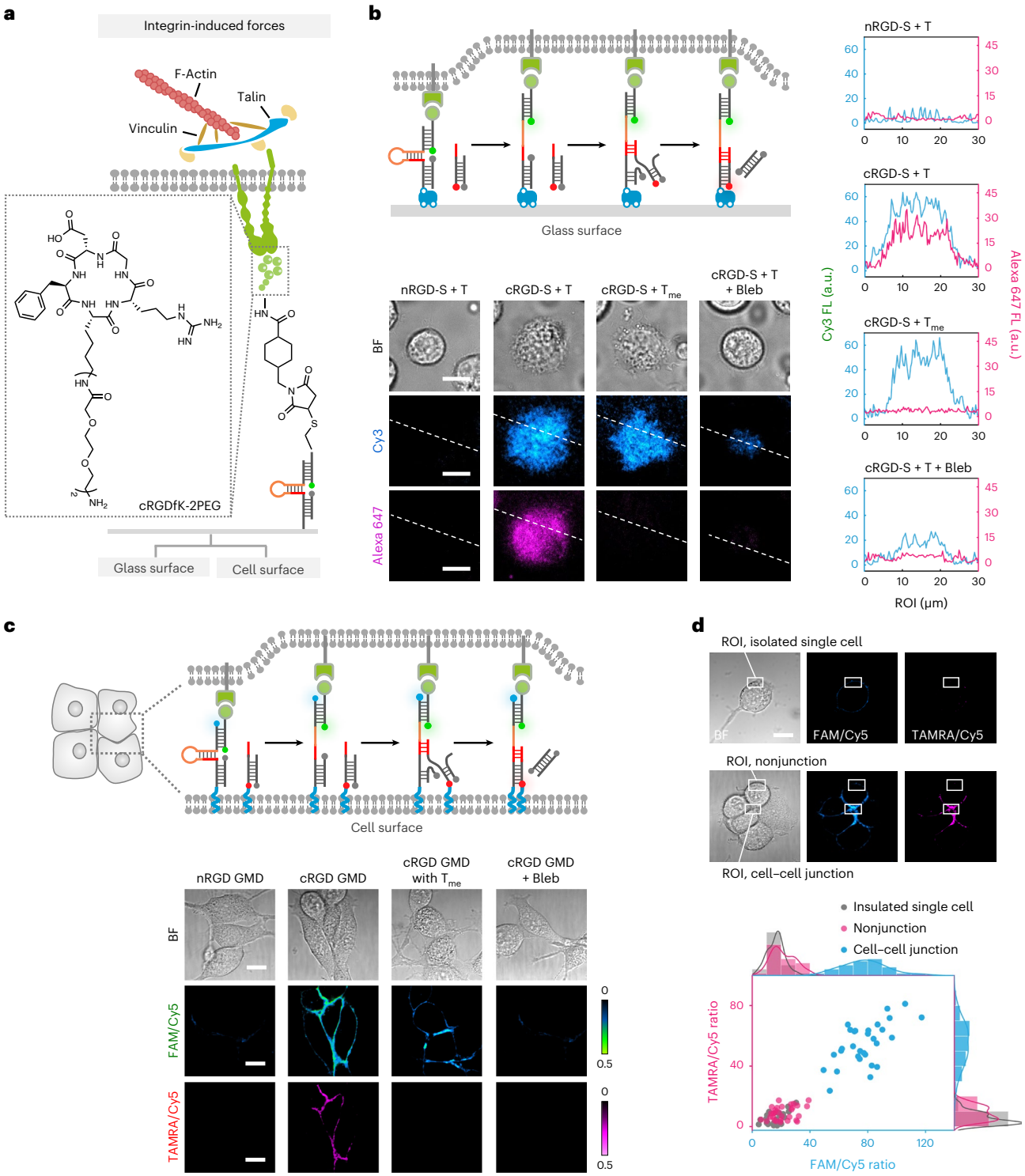

Fig. 3 | The performance of GMD to sense and transmit the cell-generated tractile force. a, Schematic diagram of the integrin-mediated tractile forces generated in cell adhesion and cell–cell interaction. **b**, The top shows a schematic to visualize the performance of GMD under the tractile forces generated during cell adhesion. The bottom shows representative TIRFM images for NIH3T3 cells spreading on the no cRGD conjugated S (nRGD-S) or cRGD-S-modified surface with soluble T or T_{me} modules. For actomyosin inhibition, cells were preincubated with Blebbistatin (10 μM) for 10 min before the cell spreading. The Cy3 and Alexa 647 channels are shown in pseudo-colors. Scale bars, 10 μm. Line profiles of the Cy3 and Alexa 647 fluorescence indicating the correlation between force-sensing events and force-transmitting events are shown in the right panel. **c**, The top shows a schematic diagram for performance evaluation of GMD under cellular tractile forces generated in cell–cell interaction. The bottom shows representative images for NIH3T3 cells engineered with nRGD GMD, cRGD GMD and cRGD GMD with T_{me}, respectively. For actomyosin inhibition, cells were preincubated with Blebbistatin (10 μM) for 10 min before cRGD GMD incubation. The normalized ratios of force-sensing signal (FAM/Cy5) and force-transmitting signal (TAMRA/Cy5) values are shown in pseudo-colors. Color bars represent normalized FAM/Cy5 and TAMRA/Cy5 ratios from 0 to 0.5, respectively. Scale bars, 10 μm. **d**, Density scatter plot shows the force-sensing signals versus the force-transmitting signals measured in the same ROI and the bars indicate their frequency of occurrence. The squares depict the representative ROI for isolated single cells, nonjunction and cell–cell junctions, respectively (n = 30 ROI from three independent experiments). Scale bars, 10 μm.

https://doi.org/10.1038/s41589-024-01572-x

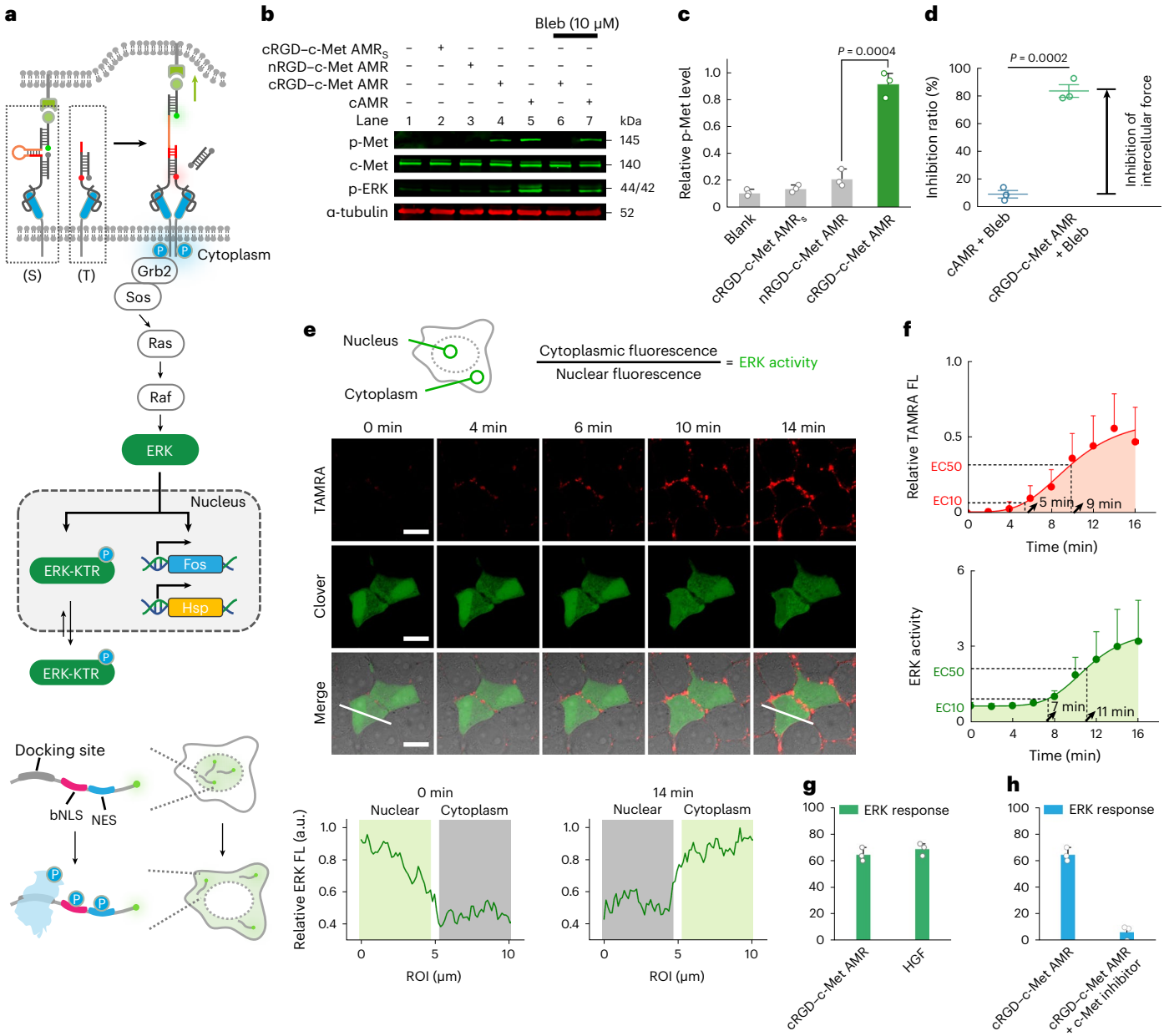

Fig. 4 | Intercellular de novo mechanotransduction by customized AMR. **a**, Schematic diagram of the AMR-tailored RTK activation for intracellular signal transduction and altered transcription program. **b**, AMR-mediated activation of c-Met and ERK signaling. The AMR-grafted HeLa cells were lysed and the c-Met phosphorylation (Tyr1234/Tyr1235) and ERK phosphorylation (Thr202/Tyr204) were analyzed using western blotting. The α-tubulin was used as an internal reference. **c**, Corresponding quantification of the relative phosphorylation level of c-Met on the western blots in **b** (normalized to the α-tubulin). $n = 3$. **d**, Quantification of the phosphorylation inhibition ratio (Supplementary Note 5) in the cRGD–c-Met AMR and cAMR groups when treated with Blebbistatin. $n = 3$. **e**, The top shows time-lapsed analysis of the AMR-activation event and ERK response of cRGD–c-Met AMR-grafted HeLa cells that were transfected with ERK-KTR Clover plasmids for 24 h. Representative images of Clover and TAMRA fluorescence (FL) channels are shown in green and red, respectively. The bottom shows linescan analysis of the ERK-KTR translocation at 0 and 14 min. Scale bars, 10 μm. **f**, Quantitative analysis of the TAMRA and ERK-KTR Clover fluorescence at the indicated time points. $n = 10$ cells. **g**, Quantitative analysis of the ERK response ratio for the cRGD–c-Met AMR and HGF treated groups. $n = 3$. **h**, Quantitative analysis of the ERK response ratio after c-Met inhibitor treatment. For c-Met inhibition, the transfected cells were pretreated with Foretinib (100 nM) for 2 h before cRGD–c-Met AMR incubation. $n = 3$. All data represent at least three independent experiments and are shown as individual data points and mean ± s.d. Significance was determined by an unpaired two-tailed Student's *t*-test.

compared with the control without cRGD (nRGD GMD). Both signals were strongly diminished by Blebbistatin or the competition with excess free cRGD ligand or soluble integrin αvβ3 protein (Fig. 3c and Supplementary Figs. 10–12), validating that the cRGD GMD is activated by actomyosin-generated force mediated by integrin. Specifically, both FAM/Cy5 and TAMRA/Cy5 signals showed heterogeneous distribution. They mainly highlighted cell–cell junctions, compared with the negligible signals at the nonjunctional region of contacting cells or the cell surface of the isolated cells (Fig. 3c). Moreover, most regions of interest (ROI) with high FAM/Cy5 ratio located at cell–cell junctions and exhibited a high TAMRA/Cy5 ratio (Fig. 3d), indicating a spatial correlation between force-sensing and force-transmitting events. These data reveal that cRGD GMD experiences the tensile forces from *trans* interaction with the neighboring cells, whereas not the *cis* interactions on the same cells[25,26]. Notably, the presence of T_{me} inhibited the TAMRA/Cy5 signal while slightly affected the FAM/Cy5 signal, verifying the

F-TSDR-dependent GMD implementation (Fig. 3c and Supplementary Fig. 10). Taken together, we validate the feasibility of GMD as an artificial mechanosensor to selectively transmit intercellular tensile forces.

AMR-tailored de novo mechanotransduction

Next, we sought to rewire the mechanotransduction in the force-receiving cells by coordinating the force-sensing and-transmission function of GMD with RTK-dimerization-mediated signaling (Fig. 4a). To prove this concept, the cRGD-S and T modules were conjugated with an aptamer motif to engineer c-Met, an RTK for the hepatic growth factor (HGF)[27], to reconstitute a chimeric AMR, namely cRGD–c-Met AMR. We installed cRGD–c-Met AMR on the A549 and HeLa cells, both highly expressed c-Met and integrin β3 (Supplementary Fig. 9 and Supplementary Table 3). The nanoscale membrane distribution of AMR was characterized by super-resolution imaging using direct stochastic optical reconstruction microscopy (dSTORM) (Supplementary Table 4). Both S and T modules displayed an inhomogeneous distribution with numerous nanodomains, similar to the pattern of c-Met (Extended Data Fig. 4). The S- and T-positive nanodomains showed high colocalization (Extended Data Fig. 5 and Supplementary Notes 1 and 2). These findings indicate that both modules of GMD largely coexist on the c-Met-rich lipid rafts[28]. The anchoring of GMD to c-Met did not affect its intercellular force-responsive performance (Extended Data Fig. 6 and Supplementary Figs. 13 and 14). The resultant AMR preferred to respond to *trans* intercellular mechanic interactions, supported by both the molecular dynamics simulations of AMR–lipid bilayer membrane system (Supplementary Fig. 15) and the high-throughput imaging analysis of AMR performance on single-cell or multicellular colonies using high-density microwell arrays (Extended Data Fig. 7 and Supplementary Fig. 16). According to the AMR design, the force-induced GMD activation hybridizes two c-Met anchoring strands to dimerize c-Met monomers, promoting autophosphorylation and downstream signaling (Fig. 4a). Using western blotting, we identified that the c-Met phosphorylation (Y1234/Y1235) was significantly elevated in the AMR-grafted cells (Fig. 4b–d and Supplementary Fig. 17). Further, the AMR-triggered downstream activation was demonstrated by the enhanced extracellular signal-regulated kinase 1/2 (ERK1/2) phosphorylation (T202/Y204) (Fig. 4b). The AMR-mediated activations of c-Met and ERK were abolished in the absence of integrin–cRGD interaction (nRGD–c-Met AMR) or T module (cRGD–c-Met AMR_S) (Fig. 4b,c). In addition, force inhibition by Blebbistatin dramatically decreased both c-Met and ERK activation in the AMR-grafted cells but hardly affected the cells stimulated by HGF and the force-independent control activated by hairpin-complementary DNA-triggered dimerization (cAMR)[29] (Fig. 4b,d and Supplementary Fig. 18). Our findings demonstrate that AMR can rewire c-Met-mediated biochemical signaling to sense intercellular tensile forces.

When phosphorylated in the RTK-mediated signal transduction, ERK acts as a regulator of gene transcription to affect diverse cellular processes (Fig. 4a). To visualize ERK response at a single-cell level, we transfected HeLa cells with ERK-kinase translocation reporter (ERK-KTR), which fused with Clover protein to sensitively probe ERK response by monitoring the nucleus-to-cytosol shuttling fluorescent signal[30] (Fig. 4e). The time-dependent ERK-KTR translocation in cRGD–c-Met AMR-grafted cells was tracked, and AMR activation was evaluated using TAMRA-BHQ2 reporters in the live-cell imaging study (Fig. 4e and Extended Data Fig. 8a). We observed that most cells exhibited enhanced ERK responses concurrent with cell–cell junctional AMR activation (Fig. 4e–h and Extended Data Fig. 8b). Quantitative analysis showed above 74% of the cells with AMR activation simultaneously coincided with activated ERK response, which was comparable to that with HGF (Fig. 4g). Remarkable activation of AMR was observed as soon as 4 min, whereas ERK response started at 6 min and a higher than twofold increase was observed after 10 min (Fig. 4f), subsequentially reaching the peak at around 30 min (Extended Data Fig. 8c,d). This finding validates that ERK activation follows the force-induced AMR activation at cell–cell junctions. Inhibition of c-Met by Foretinib significantly decreased AMR-activation-induced ERK response, suggesting the role of the kinase activity of c-Met to proceed the signaling output of AMR (Fig. 4h and Extended Data Fig. 8b). Moreover, the transcription levels of a set of downstream genes of ERK signaling were significantly upregulated on AMR activation[31], for example, the transcripts of *FOS*, *HSPA5* and *HSPB1* increased to 5.3-, 2.2- and 1.3-folds, respectively (Supplementary Fig. 19 and Supplementary Table 8). Taken together, we have reprogrammed a de novo mechanotransduction to promote RTK signaling for significant alteration in transcriptional profiles.

AMR with tunable force sensitivity

One important feature of AMR is that the hairpin motif can function as a mechano-switch, which unfolds at a given threshold force in a digital manner. We next asked whether the mechano-sensitivity of AMR could be delicately tuned. By varying the GC contents, stem lengths and loop sizes, we designed a small library of hairpins to endow AMR with different predicted force tolerances, that is, 4.5 pN (AMR_{low}), 9.8 pN (AMR_{medium}) and 16.3 pN (AMR_{high})[18] (Fig. 5a,b, Supplementary Note 4, Supplementary Fig. 20 and Supplementary Tables 5 and 7). With a predefined threshold in the hairpin motif, AMR can filter the received forces and only respond to the force exceeding the threshold, thereby transmitting via F-TSDR to promote receptor signaling. We compared the force-responsive performance of three AMRs with different thresholds. The AMR_{low}-grafted cells exhibited much higher force-sensing and force-transmitting signals at the cell–cell junctions than those with AMR_{medium} (Fig. 5c). In comparison, a negligible signal was observed under the AMR_{high}-modified cells. Previous studies have reported that integrin-mediated force ranges from 1 to 15 pN (ref. 32), supporting that it activates more AMR_{low} than AMR_{medium} but fails to affect the AMR_{high} with a threshold above the range. Accordingly, the AMR_{low}-functionalized cells exhibited the highest phosphorylation of c-Met and ERK (Fig. 5d and Supplementary Fig. 21). The c-Met phosphorylation levels were negatively dependent on the thresholds of AMR, coincident with the trend of the AMR activation at cell–cell junctions (Fig. 5e). Collectively, the force sensitivity of AMR-rewired mechanotransduction can be precisely programmed at the pN level.

Versatility of AMR to customize force input–output program

We next explored the versatility of the AMR platform in rewiring cellular signaling toward diverse cell-generated mechanical forces (Fig. 5a). Harnessing excellent modularity, AMR can endow cells with responsiveness to user-defined force inputs by easily plugging in diverse cognate ligands, for example, peptide, protein and DNA aptamer. Different from integrin for ECM adhesion, E-cadherin is a representative adhesion molecule coordinating cell–cell junctions with actin-cytoskeleton to transmit intercellular tensile forces[33]. To couple E-cadherin-mediated force, we swapped the force-reception motif of AMR with recombinant E-cadherin via a noncovalent IgG–Protein G bridge, namely, E-cad–c-Met AMR (Fig. 5f and Supplementary Fig. 22 and Supplementary Table 3). To reconstitute artificial cell–cell junctions for force transmission, we functionalized the E-cadherin$^+$c-Met$^+$ dual-positive A549 cells with E-cad–c-Met AMR, which complexed with the endogenous E-cadherin on neighboring cells (Supplementary Fig. 23). We found that both the force-sensing signal (FAM/Cy5) and AMR-activation signal (TAMRA/Cy5) were significantly increased at cell–cell junctions, much higher than the controls without E-cadherin ligand (nE-cad–c-Met AMR) (Fig. 5g and Extended Data Fig. 9a). When the cell–cell junctions were impaired by calcium chelation using EGTA, both signals were inhibited, similar to the cells treated with Blebbistatin (Fig. 5g). Moreover, E-cad–c-Met AMR-activation induced much higher c-Met phosphorylation than the controls without the E-cadherin ligand (Fig. 5h and Extended Data Fig. 9b). By contrast, Blebbistatin or EGTA strongly inhibited the AMR-mediated c-Met phosphorylation,

https://doi.org/10.1038/s41589-024-01572-x

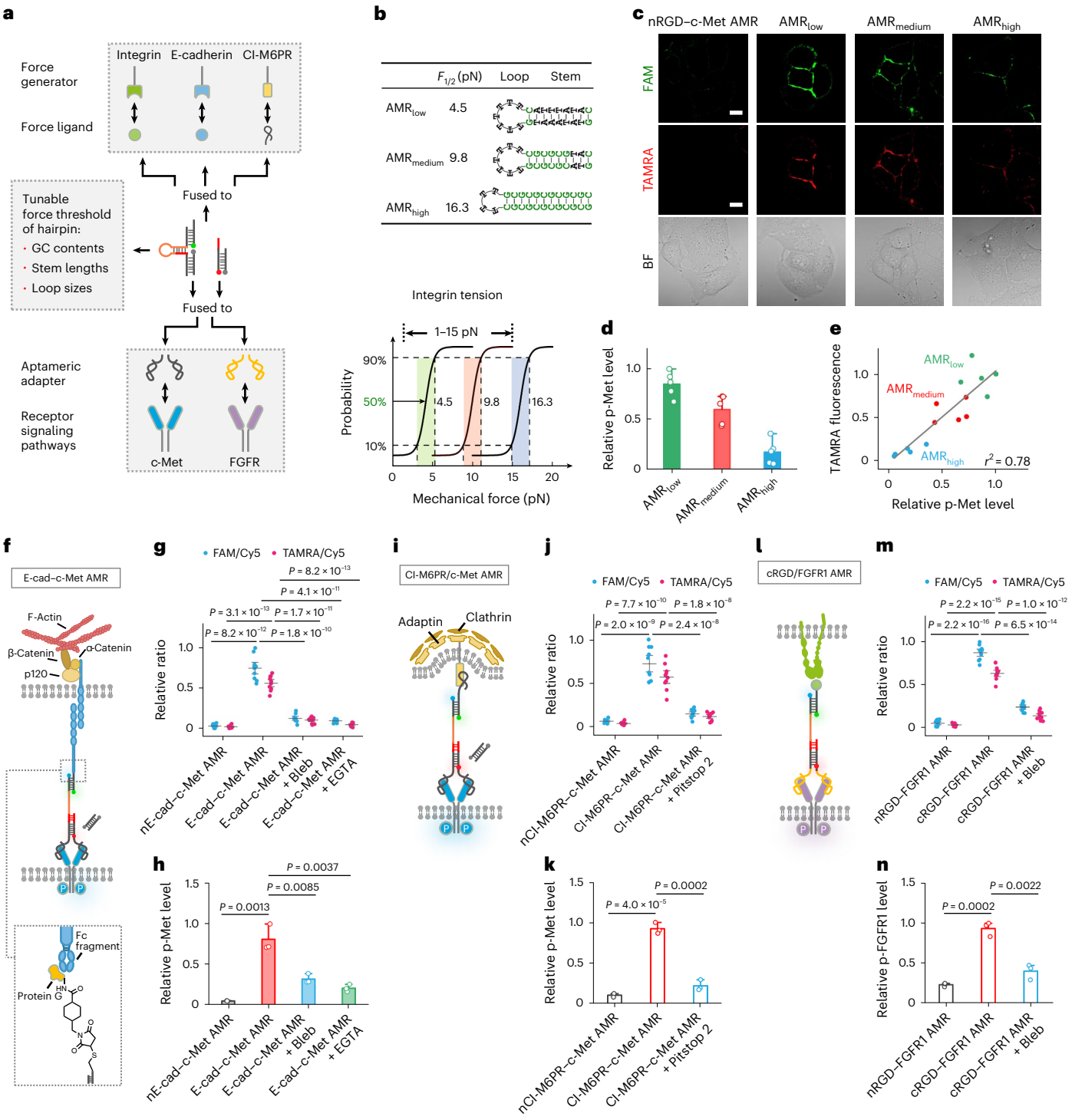

Fig. 5 | The tunability of force sensitivity and the versatility to customize the force input–output program of the AMR platform. a, Schematics of the tunable and versatile AMR designs to change force tolerances and recouple diverse inputting forces and outputting receptor signaling. **b**, The top shows a schematic of the predicted secondary structure of the folded hairpins. The bottom shows a theoretical plot showing the expected probabilities in hairpin unfolding as a function of applied forces. **c**, Representative images for the HeLa cells engineered with indicated AMRs are shown in brightfield (BF), FAM and TAMRA channels. Scale bars, 10 μm. **d**, Corresponding quantification of the relative phosphorylation levels of c-Met in the western blots as shown in Supplementary Fig. 21. $n = 5$. **e**, Correlative analysis showing the coincidence between quantified c-Met phosphorylation with the level of the AMR-activation signal, which is negatively correlated with the different force thresholds of AMRs. **f**, Schematic diagram of the E-cad–c-Met AMR to rewire E-cadherin-mediated force input into c-Met activation for A549 cells. **g**, Quantification of the relative FAM/Cy5 and TAMRA/Cy5 ratio as shown in Extended Data Fig. 9a. $n = 10$. **h**, Corresponding quantification of the relative phosphorylation of c-Met in the western blots as shown in Extended Data Fig. 9b. $n = 3$. **i**, Schematic diagram of the CI-M6PR–c-Met AMR to rewire c-Met signaling in HeLa cells toward CI-M6PR-mediated endocytic pulling forces. **j**, Quantification of the relative FAM/Cy5 and TAMRA/Cy5 ratios as shown in Extended Data Fig. 9c. $n = 10$. **k**, Corresponding quantification of the relative phosphorylation of c-Met in the western blots as shown in Extended Data Fig. 9d. $n = 3$. **l**, Schematic diagram of the cRGD–FGFR1 AMR for NIH3T3 cells. **m**, Quantification of the relative FAM/Cy5 and TAMRA/Cy5 ratios as shown in Extended Data Fig. 10a. $n = 10$. **n**, Corresponding quantification of the relative phosphorylation of FGFR1 in the western blots as shown in Extended Data Fig. 10b. $n = 3$. All data represent at least three independent experiments and are shown as individual data points and mean ± s.d. Significance was determined by unpaired two-tailed Student's t-test.

indicating that the force input is derived from actomyosin activity and mediated by E-cadherin complexes (Fig. 5h). Together, we demonstrate that E-cad–c-Met AMR can selectively translate E-cadherin-dependent force input into c-Met signaling.

Besides the actomyosin-generated forces via adhesion proteins, the forces generated during the endocytosis of membrane proteins could be used as alternative force input to activate AMR. The cation-independent mannose-6-phosphate receptor (CI-M6PR) is a cell-surface lysosome-shuttling receptor constitutively internalized via endocytosis[34]. We asked whether CI-M6PR endocytosis generated a mechanical force to activate AMR, mimicking the natural Notch receptor-mediated mechanotransduction induced by ligand endocytosis[35] (Fig. 5i). To test this idea, we developed a CI-M6PR–c-Met AMR targeting to CI-M6PR via a specific aptameric ligand (Supplementary Table 3). On CI-M6PR–c-Met AMR functionalization, the HeLa cells exhibited a much stronger intercellular AMR-activation signal than the control without the CI-M6PR-binding aptamer (nCI-M6PR–c-Met AMR) (Fig. 5j and Extended Data Fig. 9c). Consequently, CI-M6PR–c-Met AMR activation promoted significant c-Met phosphorylation, which was dramatically inhibited by Pitstop 2, a selective inhibitor of clathrin-mediated endocytosis[36] (Fig. 5k and Extended Data Fig. 9d). These results present an alternative AMR-tailored mechanotransduction toward endocytic force. Notably, this example expands the force-reception ligands from peptide or protein to nucleic acid ligand, allowing much facile AMR construction and avoiding peptide or protein-DNA conjugation.

Next, we asked whether the AMR output could be adapted to different RTKs, for example, fibroblast growth factor receptor 1 (FGFR1), which broadly regulates mitogenesis and differentiation[14] (Fig. 5a). We prepared cRGD–FGFR1 AMR via conjugating the FGFR1-specific aptamer motif with cRGD GMD to rewire FGFR1 signaling to respond to intercellular force (Fig. 5l and Supplementary Table 3). As expected, the cRGD–FGFR1 AMR-grafted NIH3T3 cell exhibited a strong AMR-activation signal on the cell–cell junction, as well as the elevated FGFR1 phosphorylation (Tyr653/Tyr654). However, both were negligible in controls without cRGD ligand (nRGD–FGFR1 AMR) or treated with Blebbistatin (Fig. 5m,n and Extended Data Fig. 10a,b). These results confirm that the modular AMR platform is customizable to diverse RTK signaling output.

AMR-customized mechanobiological function

We further exploited the signaling-reprogrammed properties of AMR to artificially regulate mechanobiological function. NSCs are crucial for neural generative therapies, but their limited natural resources require in vitro NSCs expansion, which is challenging and highly dependent on stemness maintenance[37]. In native stem cell niches, NSCs maintenance is orchestrated by basic fibroblast growth factor (bFGF)-mediated FGFR1 activation and E-cadherin-mediated intercellular adhesion[38]. To explore whether the stemness of NSCs could be maintained independent of exogenous bFGF, we rewired E-cadherin adhesion and FGFR1 signaling by developing the E-cad–FGFR1 AMR, conferring adhesion force-mediated NSCs maintenance (Fig. 6a and Supplementary Table 3). Although cultured in the medium without bFGF, E-cad–FGFR1 AMR-grafted NSCs elicited dual-channel AMR-activation signals at cell–cell junctions and induced calcium ion-dependent activation of FGFR1 and ERK signaling, demonstrating E-cadherin-mediated activation of the FGFR1-ERK signaling axis via AMR (Fig. 6b,c and Extended Data Fig. 10c,d). NSCs stemness was evaluated by immunostaining of Nestin, a NSC marker, after 3 days of incubation. AMR-grafted cells exhibited a strong Nestin-positive staining signal, comparable to the bFGF-treated group (Fig. 6d). The Nestin expression was significantly enhanced to twofold of the blank condition, suggesting NSCs stemness is maintained even at the bFGF-withdrawn condition (Fig. 6e). In comparison, the Nestin signal was much weaker in the absence of E-cadherin ligand, validating that NSCs maintenance is dependent on E-cadherin-mediated intercellular forces. Moreover, the differentiation-decoupling activity of E-cad–FGFR1 AMR was investigated by analyzing the dendrite complexity using Sholl analysis[39] (Fig. 6g,h). The result showed that E-cad–FGFR1 AMR effectively decreased the cell branching compared with the blank or nE-cad–FGFR1 AMR-treated NSCs (Fig. 6f). Taken together, we realized adhesion-mediated NSCs maintenance independent of bFGF to decouple the spontaneous neural differentiation, demonstrating an AMR-enabled designer mechanobiological function. Moreover, further implementation of AMR-rewired mechanotransductions in vivo requires improvements in the stability and cell-surface retention of GMD. Phosphorothioate modification of DNA backbone and aptamer-mediated proximity covalent conjugation might be two potential solutions (Supplementary Figs. 24–27 and Supplementary Table 6).

Discussion

Herein, we present a DNA-functionalized AMR platform enabling de novo-designed intercellular mechanotransduction. Existing synthetic mechanoreceptors, such as synNotch and synCAMs, have been developed by genetically modifying the natural Notch receptor and adhesion molecules to achieve force-induced specific gene expression and redirect natural adhesion signaling, respectively. However, a de novo strategy to reprogram a non-mechanoresponsive receptor to respond to user-defined mechanical cues remains largely unestablished. It is plausibly due to the lack of generalizable proteic mechano-transducing mechanisms since those for natural mechanoreceptors are highly diverse, specialized and not fully explained. Moreover, mechano-sensitivity tuning remains challenging because it requires a complicated trial-and-error analysis based on sophisticated protein structure-guided mutagenesis[40]. DNA-based mechanical nano-sensors, for example, tension gauge tether and molecular tension-based fluorescence microscopy sensors, present potent imaging toolkits enabling single-molecular tension detection[41–44]. These sensors are highly generalized for diverse cellular mechano-interactions. Their mechano-sensitivity can be precisely turned into a biologically relevant pN range. Although the programmability and mechanoresponsiveness of DNA molecules have been fully demonstrated in tensile force imaging, it remains rare to use DNA-based approaches to engineer cellular signaling with designer mechanobiological functions. We integrate DNA hairpin-based allosteric mechano-switch with F-TSDR to establish a generalized mechanotransduction mechanism compatible with de novo engineering of various dimerization-activated receptors, especially RTKs.

Leveraging the power of dynamic DNA nanotechnology and functional nucleic acids[45–48], our AMR strategy allows rewiring force input–output signaling with high programmability, turnability and versatility, exhibiting several unique properties. (1) Predictable and tunable force sensitivity. Harnessing the facile sequence programming of DNA hairpin mechano-switch, AMR offers a fine-tuned force tolerance with pN resolution (4–20 pN in theory)[49], allowing setting precise force sensitivity to filter the inputting cellular forces and exhibiting digital signaling responses. (2) Versatility for cellular force inputs. By conjugating diverse force-reception ligands, we demonstrated that AMR was versatile to activate cellular signaling in response to various force inputs, including but not limited to the tensile forces mediated by cell-adhesion proteins or membrane protein endocytosis. (3) Dynamic visualization of AMR actuation. Unlike proteic mechanoreceptors that require additional genetically encoded reporters for activation indication, the DNA-based AMR enables self-reporting of its mechanosensing and transmitting events through different fluorescent reporters. (4) Plug-and-play installation for diverse output receptor signaling. AMR can chemically functionalize various force-irrelevant receptors as mechanoresponsive signaling output by simply swapping specific DNA aptameric hooking motifs.

Moreover, the AMR platform presents an additional mechanical control dimension to RTKs, complementing existing chemical

https://doi.org/10.1038/s41589-024-01572-x

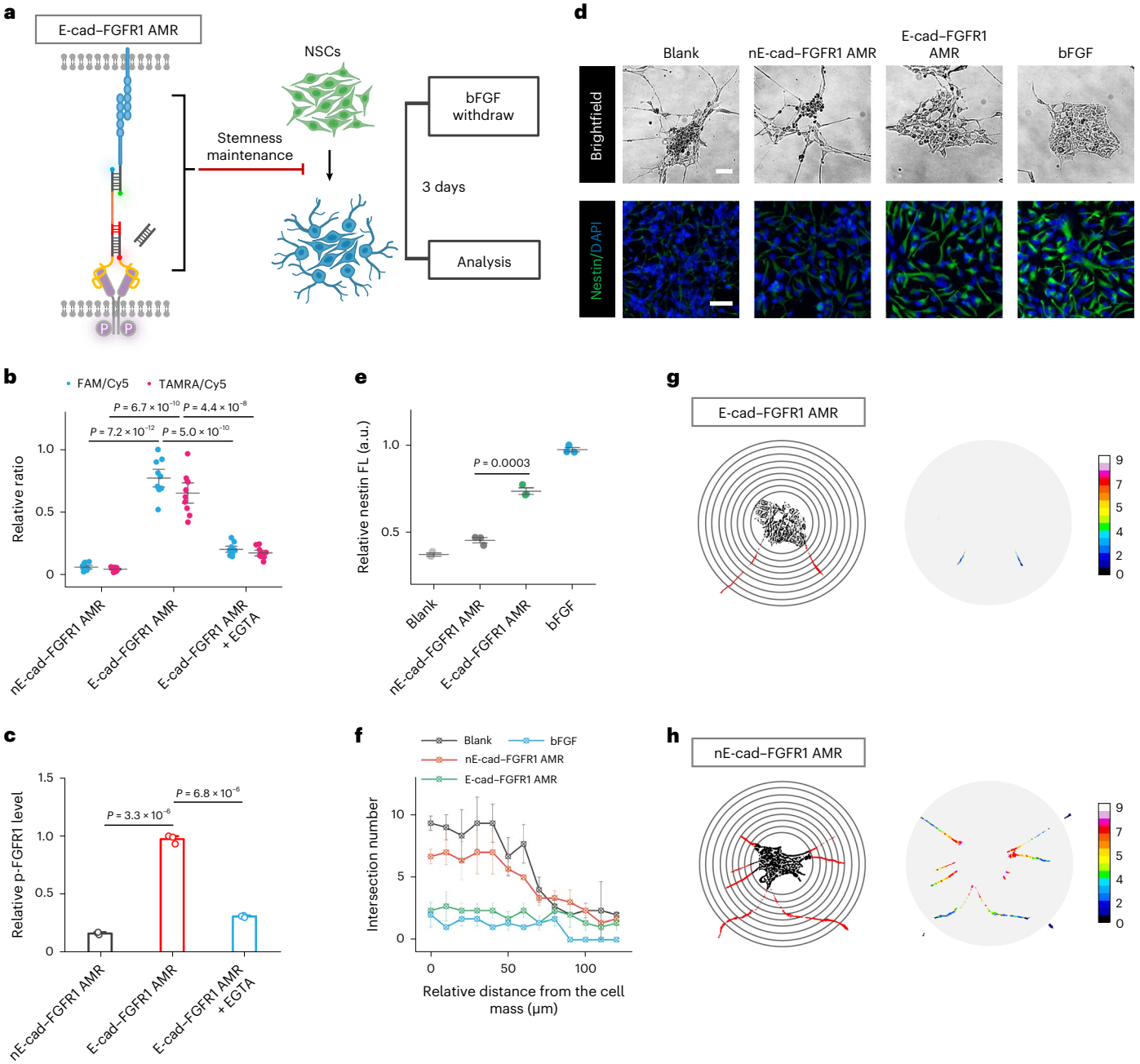

Fig. 6 | Reprogramming the AMR to customize mechanobiological function. a, Schematic diagram of the E-cad–FGFR1 AMR enabling adhesion-mediated maintenance of NSCs to decouple neural differentiation program. **b**, Quantification of the relative FAM/Cy5 and TAMRA/Cy5 ratio as shown in Extended Data Fig. 10c. $n = 10$. **c**, Corresponding quantification of the relative phosphorylation of FGFR1 in the western blots as shown in Extended Data Fig. 10d. $n = 3$. **d**, Stemness analysis of the NSCs functionalized with AMR. The NSCs were incubated with nE-cad–FGFR1 AMR, E-cad–FGFR1 AMR and bFGF, respectively, for 3 days. Representative brightfield images are shown (upper panel). Scale bar, 50 μm. The AMR-grafted NSCs after the 3-day spontaneous differentiation were subjected to immunofluorescence staining and the fluorescent images were obtained using CLSM. Representative CLSM images are presented (lower panel). Nestin (green), DAPI (blue). Scale bar, 50 μm. **e**, Quantification of the Nestin intensity (green fluorescence) as shown in **d**. Data represent mean ± s.d. ($n = 3$) from three distinct ROI (each measuring 200 × 200 μm and comprising 80–100 cells). **f**, Quantitative analysis indicating the number of intersections plotted against distance from the center of the cell cluster in the data as shown in **g** and **h**. $n = 3$. **g**,**h**, Neural differentiation analysis of the NSCs functionalized with AMR. The NSCs are incubated with E-cad–FGFR1 AMR (**g**) and nE-cad–FGFR1 AMR (**h**), respectively, for 3 days, followed by Sholl analysis to evaluate the dendrite complexity of different treatments. The representative data are shown in **g** and **h** with the radius step size of 10 μm (left). The change of color in the Sholl intersections mask represents the change of intersections (right). Color bars from 0–9 represent the number of counted intersections. All data represent at least three independent experiments and are shown as individual data points and mean ± s.d. Significance was determined by unpaired two-tailed Student's *t*-test.

and optical regulation approaches, and has the potential to open up new possibilities in the field of synthetic mechanobiology and RTK engineering[3]. This unique potential enables AMR to tailor unique mechanobiological functions, such as adhesion-mediated stemness maintenance of NSCs. Furthermore, AMR can repurpose natural RTKs to sense two layers of information, both ligand interaction and force measurement, similar to the recognition mechanism of natural mechanoreceptors, for example, the T cell antigen receptor[3].

In this context, AMR might add a band-pass force filter on biochemical recognition, enabling higher molecular recognition specificity or target identification in specific cell biological processes, for example, CI-M6PR undergoing endocytosis. The further direction is to advance the force-sensing circuit of AMR via a force-mediated DNA dynamic reaction network to rebuild the delicate natural force-discriminating strategies, for example, a catch or slip bond switch[50].

Unlike existing genetically engineered synthetic mechanoreceptors, AMR strategy uses a chemically synthetic GMD to modulate natural RTKs in a nongenetic manner, which is highly applicable for off-the-shelf applications for in situ functionalization of endogenous cells. This chemical tailoring strategy greatly simplifies mechanoreceptor engineering, but is limited by the inability to customize intracellular signaling, as well as the poor orthogonality to endogenous pathways. To address these issues, the user-defined GMDs could be further integrated with available synthetic receptor systems with dimerization-activated modes, such as MESA, GEMS and dCas9-synRs[4], to construct designer semisynthetic AMRs. These upgraded AMRs are expected to achieve orthogonal sense-and-respond mechanotransduction for desirable functions.

In summary, we harness DNA nanotechnology to develop nongenetic mechanoreceptors enabling de novo-designed mechanotransductions. This modular platform allows for versatile and flexible recoupling of various cell-generated force inputs with designated RTK signaling outputs, featuring fine-tuned force sensitivity within the biologically relevant pN range. Designer AMR-based RTK engineering offers the potential to reprogram mechanobiological functions to facilitate tissue engineering and wound healing. The AMR strategy will provide a valuable toolkit for a better understanding of mechanobiology and the future development of force-responsible cell-based therapy in regenerative medicine.

Online content

Any methods, additional references, Nature Portfolio reporting summaries, source data, extended data, supplementary information, acknowledgements, peer review information; details of author contributions and competing interests; and statements of data and code availability are available at https://doi.org/10.1038/s41589-024-01572-x.

References

1. Allen, G. M. & Lim, W. A. Rethinking cancer targeting strategies in the era of smart cell therapeutics. *Nat. Rev. Cancer* **22**, 693–702 (2022).
2. Sedlmayer, F., Aubel, D. & Fussenegger, M. Synthetic gene circuits for the detection, elimination and prevention of disease. *Nat. Biomed. Eng.* **2**, 399–415 (2018).
3. Sánchez, M. F. & Tampé, R. Ligand-independent receptor clustering modulates transmembrane signaling: a new paradigm. *Trends Biochem. Sci.* **48**, 156–171 (2023).
4. Manhas, J., Edelstein, H. I., Leonard, J. N. & Morsut, L. The evolution of synthetic receptor systems. *Nat. Chem. Biol.* **18**, 244–255 (2022).
5. Iskratsch, T., Wolfenson, H. & Sheetz, M. P. Appreciating force and shape—the rise of mechanotransduction in cell biology. *Nat. Rev. Mol. Cell Biol.* **15**, 825–833 (2014).
6. De Belly, H., Paluch, E. K. & Chalut, K. J. Interplay between mechanics and signalling in regulating cell fate. *Nat. Rev. Mol. Cell Biol.* **23**, 465–480 (2022).
7. Chen, Y., Ju, L., Rushdi, M., Ge, C. & Zhu, C. Receptor-mediated cell mechanosensing. *Mol. Biol. Cell* **28**, 3134–3155 (2017).
8. Liu, Y., Galior, K., Ma, V. P.-Y. & Salaita, K. Molecular tension probes for imaging forces at the cell surface. *Acc. Chem. Res.* **50**, 2915–2924 (2017).
9. Morsut, L. et al. Engineering customized cell sensing and response behaviors using synthetic notch receptors. *Cell* **164**, 780–791 (2016).
10. Stevens, A. J. et al. Programming multicellular assembly with synthetic cell adhesion molecules. *Nature* **614**, 144–152 (2023).
11. Zhang, D. Y. & Seelig, G. Dynamic DNA nanotechnology using strand-displacement reactions. *Nat. Chem.* **3**, 103–113 (2011).
12. Simmel, F. C., Yurke, B. & Singh, H. R. Principles and applications of nucleic acid strand displacement reactions. *Chem. Rev.* **119**, 6326–6369 (2019).
13. Del Grosso, E., Franco, E., Prins, L. J. & Ricci, F. Dissipative DNA nanotechnology. *Nat. Chem.* **14**, 600–613 (2022).
14. Lemmon, M. A. & Schlessinger, J. Cell signaling by receptor tyrosine kinases. *Cell* **141**, 1117–1134 (2010).
15. Trenker, R. & Jura, N. Receptor tyrosine kinase activation: from the ligand perspective. *Cell Signal.* **63**, 174–185 (2020).
16. Müller, D. J. et al. Atomic force microscopy-based force spectroscopy and multiparametric imaging of biomolecular and cellular systems. *Chem. Rev.* **121**, 11701–11725 (2021).
17. Kechagia, J. Z., Ivaska, J. & Roca-Cusachs, P. Integrins as biomechanical sensors of the microenvironment. *Nat. Rev. Mol. Cell Biol.* **20**, 457–473 (2019).
18. Zhang, Y., Ge, C., Zhu, C. & Salaita, K. DNA-based digital tension probes reveal integrin forces during early cell adhesion. *Nat. Commun.* **5**, 5167 (2014).
19. Bosco, A., Camunas-Soler, J. & Ritort, F. Elastic properties and secondary structure formation of single-stranded DNA at monovalent and divalent salt conditions. *Nucleic Acids Res.* **42**, 2064–2074 (2014).
20. Ma, R. et al. DNA probes that store mechanical information reveal transient piconewton forces applied by T cells. *Proc. Natl Acad. Sci. USA* **116**, 16949–16954 (2019).
21. Srinivas, N. et al. On the biophysics and kinetics of toehold-mediated DNA strand displacement. *Nucleic Acids Res.* **41**, 10641–10658 (2013).
22. You, M. et al. DNA probes for monitoring dynamic and transient molecular encounters on live cell membranes. *Nat. Nanotechnol.* **12**, 453–459 (2017).
23. Allingham, J. S., Smith, R. & Rayment, I. The structural basis of blebbistatin inhibition and specificity for myosin II. *Nat. Struct. Mol. Biol.* **12**, 378–379 (2005).
24. Belardi, B., Son, S., Felce, J. H., Dustin, M. L. & Fletcher, D. A. Cell–cell interfaces as specialized compartments directing cell function. *Nat. Rev. Mol. Cell Biol.* **21**, 750–764 (2020).
25. Zhao, B. et al. Visualizing intercellular tensile forces by DNA-based membrane molecular probes. *J. Am. Chem. Soc.* **139**, 18182–18185 (2017).
26. Zhao, B. et al. Quantifying tensile forces at cell–cell junctions with a DNA-based fluorescent probe. *Chem. Sci.* **11**, 8558–8566 (2020).
27. Uchikawa, E., Chen, Z., Xiao, G.-Y., Zhang, X. & Bai, X. Structural basis of the activation of c-MET receptor. *Nat. Commun.* **12**, 4074 (2021).
28. Seveau, S. et al. Role of lipid rafts in E-cadherin–and HGF-R/Met–mediated entry of *Listeria* monocytogenes into host cells. *J. Cell Biol.* **166**, 743–753 (2004).
29. Ueki, R., Atsuta, S., Ueki, A. & Sando, S. Nongenetic reprogramming of the ligand specificity of growth factor receptors by bispecific DNA aptamers. *J. Am. Chem. Soc.* **139**, 6554–6557 (2017).
30. Kudo, T. et al. Live-cell measurements of kinase activity in single cells using translocation reporters. *Nat. Protoc.* **13**, 155–169 (2018).
31. Gille, H., Sharrocks, A. D. & Shaw, P. E. Phosphorylation of transcription factor p62TCF by MAP kinase stimulates ternary complex formation at c-fos promoter. *Nature* **358**, 414–417 (1992).
32. Liu, Y., Yehl, K., Narui, Y. & Salaita, K. Tension sensing nanoparticles for mechano-imaging at the living/nonliving interface. *J. Am. Chem. Soc.* **135**, 5320–5323 (2013).
33. Lecuit, T. & Yap, A. S. E-cadherin junctions as active mechanical integrators in tissue dynamics. *Nat. Cell Biol.* **17**, 533–539 (2015).

34. Banik, S. M. et al. Lysosome-targeting chimaeras for degradation of extracellular proteins. *Nature* **584**, 291–297 (2020).
35. Gordon, W. R. et al. Mechanical allostery: evidence for a force requirement in the proteolytic activation of notch. *Dev. Cell* **33**, 729–736 (2015).
36. von Kleist, L. et al. Role of the clathrin terminal domain in regulating coated pit dynamics revealed by small molecule inhibition. *Cell* **146**, 471–484 (2011).
37. Diamandis, P. et al. Chemical genetics reveals a complex functional ground state of neural stem cells. *Nat. Chem. Biol.* **3**, 268–273 (2007).
38. Karpowicz, P. et al. E-Cadherin regulates neural stem cell self-renewal. *J. Neurosci.* **29**, 3885–3896 (2009).
39. Ferreira, T. A. et al. Neuronal morphometry directly from bitmap images. *Nat. Methods* **11**, 982–984 (2014).
40. Sloas, D. C., Tran, J. C., Marzilli, A. M. & Ngo, J. T. Tension-tuned receptors for synthetic mechanotransduction and intercellular force detection. *Nat. Biotechnol.* **41**, 1287–1295 (2023).
41. Wang, X. & Ha, T. Defining single molecular forces required to activate integrin and notch signaling. *Science* **340**, 991–994 (2013).
42. Ma, V. P.-Y. & Salaita, K. DNA nanotechnology as an emerging tool to study mechanotransduction in living systems. *Small* **15**, 1900961 (2019).
43. Li, H. et al. A reversible shearing DNA probe for visualizing mechanically strong receptors in living cells. *Nat. Cell Biol.* **23**, 642–651 (2021).
44. Zhang, Z. et al. Programmable integrin and N-cadherin adhesive interactions modulate mechanosensing of mesenchymal stem cells by cofilin phosphorylation. *Nat. Commun.* **13**, 6854 (2022).
45. Shaw, A. et al. Spatial control of membrane receptor function using ligand nanocalipers. *Nat. Methods* **11**, 841–846 (2014).
46. Li, J., Green, A. A., Yan, H. & Fan, C. Engineering nucleic acid structures for programmable molecular circuitry and intracellular biocomputation. *Nat. Chem.* **9**, 1056–1067 (2017).
47. Mills, A. et al. A modular spring-loaded actuator for mechanical activation of membrane proteins. *Nat. Commun.* **13**, 3182 (2022).
48. Saminathan, A. et al. A DNA-based voltmeter for organelles. *Nat. Nanotechnol.* **16**, 96–103 (2021).
49. Woodside, M. T. et al. Nanomechanical measurements of the sequence-dependent folding landscapes of single nucleic acid hairpins. *Proc. Natl Acad. Sci. USA* **103**, 6190–6195 (2006).
50. Prezhdo, O. V. & Pereverzev, Y. V. Theoretical aspects of the biological catch bond. *Acc. Chem. Res.* **42**, 693–703 (2009).

Methods

Oligonucleotides

All oligonucleotides for the construction of the DNA–protein chimeric platform (detailed sequences listed in Supplementary Tables 1–6) and real-time quantitative PCR (qPCR) experiments (detailed sequences listed in Supplementary Table 8) were custom-synthesized by Sangon Biotech Co., Ltd.

Cell culture and transfection

All cell lines were cultured at 37 °C in a humid atmosphere with 5% CO_2. HeLa cells (ATCC, cat. no. CCL-2) were cultured in DMEM (Gibco, cat. no. 11965092) with 10% FBS (Biological Industries, cat. no. 04-001-1A) and 1% penicillin and streptomycin (NCM Biotech, cat. no. C125C5). A549 (ATCC, cat. no. CCL-185) cells were cultured in RPMI1640 (Gibco, cat. no. 11875119) with 10% FBS and 1% penicillin and streptomycin. NIH3T3 (ATCC, cat. no. CRL-1658) mouse embryonic fibroblasts were cultured in DMEM with 10% super newborn calf serum (Sangon Biotech, cat. no. E510004) and 1% penicillin and streptomycin.

To visualize the ERK response, HeLa cells were transfected with the ERK-kinase translocation reporter (Addgene, cat. no. 59138) using Lipo8000 (Beyotime, cat. no. C0533) transfection reagent based on standard protocols provided by Beyotime. Afterward, the cells were incubated with 400 nM cRGD–c-Met AMR in HEPES buffered saline solution for 30 min. For positive control, the transfected cells were incubated with 2 nM HGF (Sino Biological, cat. no. 10463-HNAS) for 30 min. For c-Met inhibition, the transfected cells were pretreated with 100 nM Foretinib (Solarbio, IF0490) for 2 h before cRGD–c-Met AMR incubation. Real-time live-cell images were collected at 488 and 561 nm with CLSM (Nikon Ti-E controlled by NIS Elements AR) using a ×60 oil immersion objective.

Preparation and characterization of cRGD-S

To prepare the cRGD-S, the cRGD-modified DNA strand (cRGD-Sf) was synthesized according to the previous protocol[25]. Briefly, cRGDfK (synthesized by Sangon Biotech) was conjugated to the single-stranded DNA (ssDNA) strand using a hetero-bifunctional crosslinker, sulfo-SMCC (Macklin, cat. no. C15454530). Sulfo-SMCC has maleimide and *N*-hydroxysuccinimide (NHS) ester groups on two ends, which react with the thiol group on thiol-modified DNA and amine on cRGDfK, respectively. Before the thiol–maleimide reaction, 25 µl of 200 µM DNA was deprotected by Tris-(2-carboxyethyl)-phosphine hydrochloride (TCEP) (Aladdin, cat. no. T107252) (100 mM in PBS containing 50 mM EDTA, pH 7.2) at room temperature for 1 h. The DNA solution was purified with a Bio-spin 6 column (Bio-Rad, cat. no. 732-6221) in PBS buffer to remove excess TCEP. Then, the thiol-modified DNA was mixed with 5 µl of sulfo-SMCC (23 mM, dissolved in ultrapure water) and incubated at room temperature for 30 min, followed by purification with the Bio-spin 6 column again. Afterward, DNA linked to the crosslinker and 10 µl of cRGDfK (10 mg ml^{-1} in PBS, pH 7.2) were immediately mixed and kept at 4 °C overnight. The RGD conjugated DNA was purified with the Bio-spin 6 column to give the final product. To prepare the cRGD-S assembly, cRGD-Sf, Sh and Sb were mixed in PBS or HEPES at a concentration of 100 nM and denatured at 75 °C for 5 min, followed by a renaturation step in which the temperature was allowed to return to 5 °C at a rate of 1.3 °C min^{-1}. To confirm the formation of DNA structures, native-PAGE was carried out in 1× Tris-borate-EDTA buffer at 100 V for 1.5 h. Afterward, the gel was stained by SYBR Green II for 30 min and imaged using Azure Biosystems 600 controlled by the Azure Imaging System.

Functionalization of the glass substrate with cRGD-S

According to the previously described protocol[18], the cRGD-S module was immobilized on a glass substrate through streptavidin–biotin interactions. Glass coverslips were sonicated in Nanopure water for 10 min and then etched with piranha (a 3:1 mixture of sulfuric acid and hydrogen peroxide) for 30 min to achieve a hydroxylated surface. After rinsing six times with Nanopure water and three times with EtOH, the coverslips were functionalized with amine groups by incubating the coverslips with 1% v/v (3-aminopropyl) triethoxysilane solution (APTES, Energy Chemical, cat. no. E080931) in ethanol for 1 h. The coverslips were then rinsed three times in EtOH and dried under nitrogen. To cure the APTES layer, coverslips were baked at 80 °C for 20 min. Subsequently, the coverslips were incubated with 2 mg ml^{-1} NHS-biotin (Meryer, cat. no. M14735) in dimethylsulfoxide overnight, followed by rinsing three times with EtOH and dried under nitrogen. Then, the coverslips were washed with PBS three times, incubated with 100 mg ml^{-1} bovine serum albumin (BSA, Sangon Biotech, cat. no. A600332) for 30 min and washed again with PBS. Then, 1 mg ml^{-1} streptavidin (Macklin, cat. no. S6367) was added to the coverslips and incubated for 45 min at room temperature followed by washing with PBS. Finally, cRGD-S (100 nM) in PBS was added onto the coverslips and incubated at room temperature for 1 h. cRGD-S-modified coverslips were washed with PBS to remove nonspecifically bound DNA. These modified coverslips were rinsed in PBS before cell experiments.

TIRFM

NIH3T3 cells were plated at low density on the cRGD-S-modified substrates and imaged in the serum-free DMEM medium containing 200-nM T modules at room temperature. For the actomyosin inhibition, cells were pretreated with 10 µM Blebbistatin for 10 min before imaging. Images were acquired on a Leica DMi8 Infinity TIRFM equipped with high-powered lasers (561 and 640 nm), a ×100 1.46 numerical aperture (NA) oil objective and an EMCCD camera. Penetration depth was 150 nm, and laser intensity and exposure parameters remained constant for all samples. The TIRF microscopy images were operated by LAS X software and processed using ImageJ (Supplementary Fig. 8).

AFM cantilever functionalization

Silicon nitride cantilevers (Bruker, cat. no. MLCT-O10) were incubated with 50 µg ml^{-1} recombinant integrin αvβ3 protein (Sino Biological, cat. no. CT098-H08H) for 2 h at 37 °C and then blocked by 1% BSA in PBS for 2 h at 37 °C. The modified cantilevers were washed with PBS and used for AFM tests immediately.

Force spectroscopy measurements

AFM experiments were performed on Nanowizard II AFM (Bruker) controlled by JPK BioAFM software. A thermal noise fluctuation method was used to calibrate the spring constant of Bruker MLCT cantilevers. The FE cycles were performed in the Dulbecco PBS solution. The integrin-modified cantilever was brought into contact with the cRGD-S-modified substrate under a compression force of 500 pN for 20 ms, and then retracted with a velocity of 300 nm s^{-1}. All of the FE curves were analyzed using JPK SPM data processing.

Combined AFM and CLSM

To image the fluorescent signals on the cell surface after AFM scanning, Nanowizard II AFM was coupled with an inverted confocal microscope (Zeiss, cat. no. LSM710). The HeLa cells were seeded on a 35-mm confocal dish for 24 h and then incubated with 1 µM cholesterol-conjugated cRGD-S and T modules in Dulbecco PBS for 20 min. Then, the cantilever is raster-scanned across the cell surface at a resolution of 16 × 16 pixels over a scanning area of 5 × 5 $µm^2$. The compression force was set to 500 pN, and both the approach and retraction velocity were set to 300 nm s^{-1}. Images were collected using ZEN using a ×40 lens with 488, 561 and 647-nm lasers and processed by ImageJ.

Preparation and characterization of E-cadherin-S

To prepare the E-cadherin-S, the Protein G-modified DNA strand (ProG-Sf) was first synthesized as described previously[51]. Here, 20 µl of thiol-modified ssDNA (1 mM) was mixed with 5 µl of TCEP (50 mM

in PBS containing 50 mM EDTA at pH 7.2) for 30 min at room temperature. After purifying the DNA with Bio-spin 6 column, 1.5 µl of 23 mM sulfo-SMCC was added and incubated for 1 min. Then, the DNA solution was incubated with 10 µl of Protein G (Beyotime, cat. no. P5030) at 4 °C overnight. The synthesized ProG-Sf product was purified using Dynabead (Invitrogen, cat. no. 10103D) through His-tag purification, followed by a buffer exchange process using Bio-spin 6 column. Afterward, the ProG-Sf was incubated with the prehybridized Sh and Sb strands at a 1:1 ratio at 4 °C overnight. This assembly was then incubated with equimolar hFc-tagged E-cadherin (Sino Biological, cat. no. 10204-H02H) at 4 °C for 2 h to give the final E-cadherin-S construct. All of the stepwise synthesized DNA constructs were confirmed by native-PAGE.

Fluorescent live-cell imaging

To investigate the performance of cRGD GMD under cell-generated force, NIH3T3 cells were seeded on a 35-mm confocal dish for 24 h and then incubated with 1 µM cholesterol-modified cRGD-S and T modules (together as cRGD GMD) in HEPES buffered saline solution for 30 min. For the actomyosin inhibition, cells were pretreated with 10 µM Blebbistatin (Aladdin, cat. no. B129580) for 10 min before cRGD GMD functionalization. In the competition assay, 100 µM cRGDfk peptide or 1 µM integrin αvβ3 protein in the HEPES was added after 30 min GMD functionalization.

To evaluate the performance of the cRGD–c-Met AMR or cRGD–FGFR1 AMR, HeLa, A549 or NIH3T3 cells were seeded on a 35 mm confocal dish for 24 h and incubated with 400 nM cRGD–c-Met AMR or cRGD–FGFR1 AMR in PBS for 30 min. For the actomyosin inhibition, cells were pretreated with Blebbistatin (10 µM) for 10 min before AMR functionalization.

To evaluate the performance of the E-cad–c-Met AMR or E-cad–FGFR1 AMR, A549 or NSCs were seeded on a 35-mm confocal dish for 24 h and incubated with 400 nM E-cad–c-Met AMR or E-cad–FGFR1 AMR in PBS for 30 min. For the E-cadherin inhibition assay, cells were pretreated with 5 mM EGTA (Beyotime, ST068) for 30 min before AMR functionalization.

To evaluate the performance of the CI-M6PR–c-Met AMR, HeLa cells were seeded on a 35-mm confocal dish and then incubated with 400 nM CI-M6PR–c-Met AMR in PBS for 30 min. For the endocytosis inhibition, cells were pretreated with 30 µM Pitstop 2 (Sigma-Aldrich, cat. no. SML1169) for 30 min before AMR functionalization. In the competition assay, PBS supplemented with 1 µM soluble CI-M6PR aptamer was added and incubated for an additional 30 min.

After indicated incubation, excess DNA was removed by washing twice with PBS, and cells were imaged in HEPES or PBS. All of the fluorescent live-cell images were collected at 488, 561 and 647 nm with CLSM. All fluorescent images were processed, analyzed and quantified using ImageJ.

dSTORM imaging

To image the subcellular location of c-Met with immunofluorescence, A549 cells were fixed with 6% paraformaldehyde (PFA) + 1.5% glutaraldehyde at room temperature for 10 min, blocked with 3% BSA for 30 min and stained with the primary Met antibody (1:1,500) at room temperature for 60 min. Subsequently, the samples were washed with PBS three times and stained with Alexa Fluor 647-labeled goat antirabbit secondary antibody (Beyotime, cat. no. A0468, 1:25) for 60 min at room temperature. Finally, the cells were washed and immersed in dSTORM imaging buffer containing glucose oxidase, catalase and beta-mercaptoethanol.

For single-channel dSTORM imaging of S or T on live cells, A549 cells incubated with Alexa Fluor 532-labeled S (400 nM) or Alexa Fluor 647-labeled T (400 nM) at 37 °C for 15 min and fixed with 6% PFA + 1.5% glutaraldehyde at room temperature for 10 min, followed by PBS washing three times. Subsequently, the cells were immersed in the dSTORM imaging buffer. For dual-color S and T imaging, the cells were incubated with both Alexa Fluor 532-labeled S (400 nM) and Alexa Fluor 647-labeled T (400 nM) at 37 °C for 15 min and fixed with 6% PFA + 1.5% glutaraldehyde at room temperature for 10 min, followed by PBS washing three times. Subsequently, the cells were immersed in the dSTORM imaging buffer.

dSTORM imaging was performed on an Abbelight STORM Imaging System controlled by NEO software with a ×100 1.49 NA TIRF lens using a 532-nm laser and a 647-nm laser. For single-color dSTORM imaging, the sample was excited with either a 532-nm laser to excite the Alexa Fluor 532-labeled S or a 647-nm laser to excite the Alexa Fluor 647-labeled T or c-Met, respectively. For dual-color dSTORM, the samples were first excited with a 647-nm laser to excite the Alexa Fluor 647-labeled T and then photoactivated with a 532 nm laser to excite the Alexa Fluor 532-labeled S. A time series of 10,000 frames per cell were recorded with a 20-ms exposure time for the reconstruction of the super-resolution image. Performing one single or dual-color dSTORM imaging took less than 10 min. During imaging, an auto-focus lock was used to eliminate the *z* drift, and the data postprocessing by ThunderSTORM[52] was used to correct the *xy* drift.

Surface plasmon resonance assay

For the surface plasmon resonance assay, recombinant c-Met protein (10692-H03H) and recombinant IgG1-Fc Protein (10702-HNAH) were purchased from Sino Biological. Series S Sensor Chip CM5 (Cytiva) was placed in the chip tank of the Biacore 8K instrument controlled by Biacore 8K Control Software. Channels of the chip were cleaned using 50 mM NaOH and then activated by 1-(3-dimethylaminopropyl)-3-ethylcarbodiimide hydrochloride and NHS. Then, c-Met protein (diluted to 20 µg ml^{-1} with pH 5.5 NaAc) and Fc protein (diluted to 20 µg ml^{-1} with pH 5.5 NaAc) as controls were immobilized, followed by treatment with pH 8.5 ethanolamine-HCl to deactivate unreacted carboxyl groups. S, T and S/T (Sf–Sh–Te hybrid) with gradient concentrations (5–640 nM) were injected at a flow rate of 30 µl min^{-1} for 120 s, followed by 360 s of dissociation in a running buffer. The relative response was recorded in the sensorgram, and the data were fit with Biacore Insight Evaluation Software to obtain the association rate constant K_{on}, dissociation rate constant K_{off} and equilibrium dissociation constant K_d.

Flow cytometry

To analyze the binding of S and T to cell-surface c-Met of live cells, HeLa cell suspensions (1×10^5) were incubated with Cy5-labeled S or Cy5-labeled T (0–200 nM) in PBS for 20 min, respectively. The binding performance of S and T were analyzed by CytoFLEX flow cytometry controlled by CytExpert (Beckman) and analyzed using FlowJo after washing with PBS. The dissociation constant of S and T to c-Met on the cell surface was determined using the equation[53],

$$\text{Bound fraction} = \frac{F - F_0}{F_{max} - F_0} = \frac{[\text{S or T}]}{[\text{S or T}] + K_d}$$

where F_0 and F_{max} represent the minimum or maximum change in fluorescent intensity, respectively, and K_d is the dissociation constant.

Single-cell and multicell high-density microarray

To visualize the performance of AMR on isolated single- and multicell colonies, we fabricated a perforated polydimethylsiloxane (PDMS) miniaturized high-density microwell array chip[54]. The PDMS stencil layer (100-µm pore size, 10 × 10 wells) was cleaned with ultra-sonication in ethanol and attached evenly onto a glass surface of a 35-mm confocal dish by curing at 80 °C for 15 min. After washing and immersing with cell culture medium to make the surface hydrophilic, the microwell chip was ready to be used to capture and culture cells. The HeLa cell suspension with a density of 1×10^4 cells per ml was added to the PDMS microchip and fell into the microwells by gravity to give single-cell

distribution. The cell suspension with a density of 1×10^6 cells per ml was added to give multicell distribution. The cells were allowed to be adhered for 12 h and then incubated with 400 nM cRGD–c-Met AMR in PBS for 30 min. After washing with PBS, the cells in each microwell were imaged by CLSM.

Immunoblots

Cells were starved in a medium supplemented with 0.2% FBS for 16 h and incubated with DNA for 15 min at 5% CO_2 and 37 °C. After the incubation, cells were washed twice with precooling PBS and lysed. The cell lysates were centrifuged at 14,000*g* for 10 min at 4 °C, and then the supernatants were recovered. The protein samples were separated by 8% SDS–PAGE and transferred to a nitrocellulose membrane using a semidry electrophoretic transfer unit. The membranes were blocked with 5% BSA-PBST for 1 h at room temperature and incubated with the primary antibody overnight at 4 °C and then incubated with the secondary antibody for 1 h at room temperature The primary antibodies of Met (8198, 1:1,000), integrin β3 (13166, 1:1,000), phospho-Met (Tyr1234/Tyr1235, 3077, 1:1,000), phospho-FGFR1 (Tyr653/Tyr654, 52928, 1:1,000) and phospho-p44/42 MAPK (Thr202/Tyr204, 4370, 1:2,500) were obtained from Cell Signaling Technology. The anti-CDH1 rabbit polyclonal antibody (E-CAD, D260656, 1:1,000) was purchased from Sangon Biotech. The α-tubulin monoclonal antibody (18073008-1, 1:2,500) was purchased from Cellway Bio. The IRDye 680RD goat antimouse secondary antibody (925-68070, 1:10,000) and IRDye 680RD goat antirabbit secondary antibody (925-68071, 1:10,000) were obtained from LI-COR. The HRP-conjugated goat antirabbit secondary antibody (31460, 1:2,500) and HRP-conjugated goat antimouse secondary antibody (31430, 1:2,500) were obtained from Thermo Fisher Scientific. Finally, the western blotting images were obtained using the LI-COR Odyssey Infrared Imaging System controlled by Image Studio or Azure Biosystems 600 controlled by Azure Imaging System.

Real-time qPCR

The transcriptional levels of genes downstream of ERK activation were determined by real-time qPCR using glyceraldehyde 3-phosphate dehydrogenase messenger RNA as an internal reference. Cells grown on a 6-cm dish were starved in a medium supplemented with 0.2% FBS for 16 h and then stimulated with cRGD–c-Met AMR for 0, 12 and 24 h at 5% CO_2 and 37 °C. Total RNAs were extracted with the RNAprep pure Cell/Bacteria Kit (TIANGEN, cat. no. DP430) by following the manufacturer's instructions. The extracted RNAs were quantified using the Nanodrop spectrophotometer and then reverse-transcribed to complementary DNAs using Evo M-MLV Reverse Transcriptase Synthesis Kit (Accurate Biology, AG11705). Real-time PCR was performed using a standard ChamQ Universal SYBR qPCR Master Mix (Vazume, Q711) protocol on an Applied Biosystems QuantStudio 7 Flex controlled by Real-Time PCR. The sequences of primers are listed in Supplementary Table 8.

NSCs culture and differentiation

NSCs were obtained from the Cellway Bio and cultured at 37 °C and 5% CO_2 in DMEM supplemented with N2, B27 and 10 ng ml^{-1} bFGF (Thermo Fisher Scientific, cat. nos. 17502048, 17504044 and PHG0368). For differentiation assay, NSCs were plated at 35-mm dishes and cultured without bFGF. Following the removal of bFGF, NSCs were treated with nE-cad–FGFR1 AMR or E-cad–FGFR1 AMR for 3 days. Then, the cells were fixed with 4% PFA for 15 min and permeabilized with 0.5% Triton X-100 for 30 min at room temperature. Subsequently, samples were blocked in 10% normal goat serum for 1 h and incubated overnight at 4 °C with primary Nestin rabbit monoclonal antibody (Beyotime, cat. no. AF2215, 1:200). Immunoreactivity was detected with Alexa Fluor 488-labeled goat antirabbit secondary antibody (Beyotime, cat. no. A0423, 1:500). The cell nuclei were stained with 4,6-diamidino-2-phenylindole (DAPI) (Beyotime, cat. no. C1005) for 5 min. The brightfield and fluorescent images were acquired on the BioTek Cytation 5 controlled by Gen5. The images were analyzed and quantified using ImageJ with the Sholl Analysis plug-in. Sholl analysis creates concentric ROI selections with a specified radial increase in binarized brightfield images, followed by quantification using the plug-in algorithm. The neurites crossing every single ring and each neurite that crosses a specific circle is counted as one intersection.

Serum stability assessment

The stability of S and T was investigated in PBS and serum. S, T and control ssDNA with random sequence and similar monomeric length (mer) were incubated in PBS or DMEM medium supplemented with 10% FBS for durations of 0, 2, 4, 6, 12 or 24 h at 37 °C. The stability of the S and T modules were further examined in the cell culture medium in the presence of 1×10^5 cultured c-Met^- NIH3T3 cells, which exclusively investigated the stability, avoiding the effect of aptameric target-binding-caused cell adsorption and endocytosis. Subsequently, the serum stability for each condition was analyzed by 8% native-PAGE gel electrophoresis, run for 70 min at 110 V. The gel was then stained by SYBR Green II for 30 min and imaged using an Azure Biosystems 600 controlled by Azure Imaging System.

Statistics and reproducibility

All data in graphs were presented as means ± standard deviation (s.d.) from at least three biologically independent experiments. All micrograph data (confocal, TIRF and dSTORM images) are representative of at least three biologically independent experiments with similar results. Statistical significance was determined by unpaired two-tailed Student's *t*-test, and $P < 0.05$ was considered to be statistically significant. NS indicates not significant.

Reporting summary

Further information on research design is available in the Nature Portfolio Reporting Summary linked to this article.

Data availability

All data supporting the findings of this study are available within the article and its Supplementary Information. Source data are provided with this paper.

References

51. Wang, X. et al. Constructing modular and universal single molecule tension sensor using protein G to study mechanosensitive receptors. *Sci. Rep.* **6**, 21584 (2016).
52. Ovesný, M., Křížek, P., Borkovec, J., Švindrych, Z. & Hagen, G. M. ThunderSTORM: a comprehensive ImageJ plug-in for PALM and STORM data analysis and super-resolution imaging. *Bioinformatics* **30**, 2389–2390 (2014).
53. Ricci, F., Vallée-Bélisle, A., Porchetta, A. & Plaxco, K. W. Rational design of allosteric inhibitors and activators using the population-shift model: in vitro validation and application to an artificial biosensor. *J. Am. Chem. Soc.* **134**, 15177–15180 (2012).
54. Bai, R. et al. Paper-based 3D scaffold for multiplexed single cell secretomic analysis. *Anal. Chem.* **90**, 5825–5832 (2018).

Acknowledgements

We thank Y. Lu and Y. H. Ji (Dalian Institute of Chemical Physics, Chinese Academy of Sciences) for their technical support in the preparation of high-density microwell array chips. We thank H. D. Wang and J. Gao (Changchun Institute of Applied Chemistry, Chinese Academy of Sciences) for providing technical assistance on dSTORM imaging and data analysis. We thank N. Cai (Cellway Biotechnology Co., Ltd) for technical discussions in cell culture of NSCs. This research was supported by the National Key Research and Development Program of China (grant nos. 2020YFA0907500 and 2021YFA0910100 to Z.N.) and the National Natural Science Foundation of China (grant nos. 22034002 and 92253304 to Z.N., 22177030 to H.h.W.).

Author contributions

Z.N. conceived and designed the project. S.Y., H.h.W. and Z.N. designed, and S.Y. performed the experiments. M.L., S.L., D.T. and X.Z. provided technical assistance for AFM-related experiments. S.Y., M.W., K.C., H.h.W. and Z.N. analyzed the data. Z.N., H.h.W, and S.Y. wrote the manuscript and supervised the project. All authors read and commented on the manuscript.

Competing interests

The authors declare no competing interests.

Additional information

Extended data is available for this paper at https://doi.org/10.1038/s41589-024-01572-x.

Supplementary information The online version contains supplementary material available at https://doi.org/10.1038/s41589-024-01572-x.

Correspondence and requests for materials should be addressed to Zhou Nie.

Peer review information *Nature Chemical Biology* thanks Chung Hang Jonathan Choi, Anna Leopold and the other, anonymous, reviewer(s) for their contribution to the peer review of this work.

https://doi.org/10.1038/s41589-024-01572-x

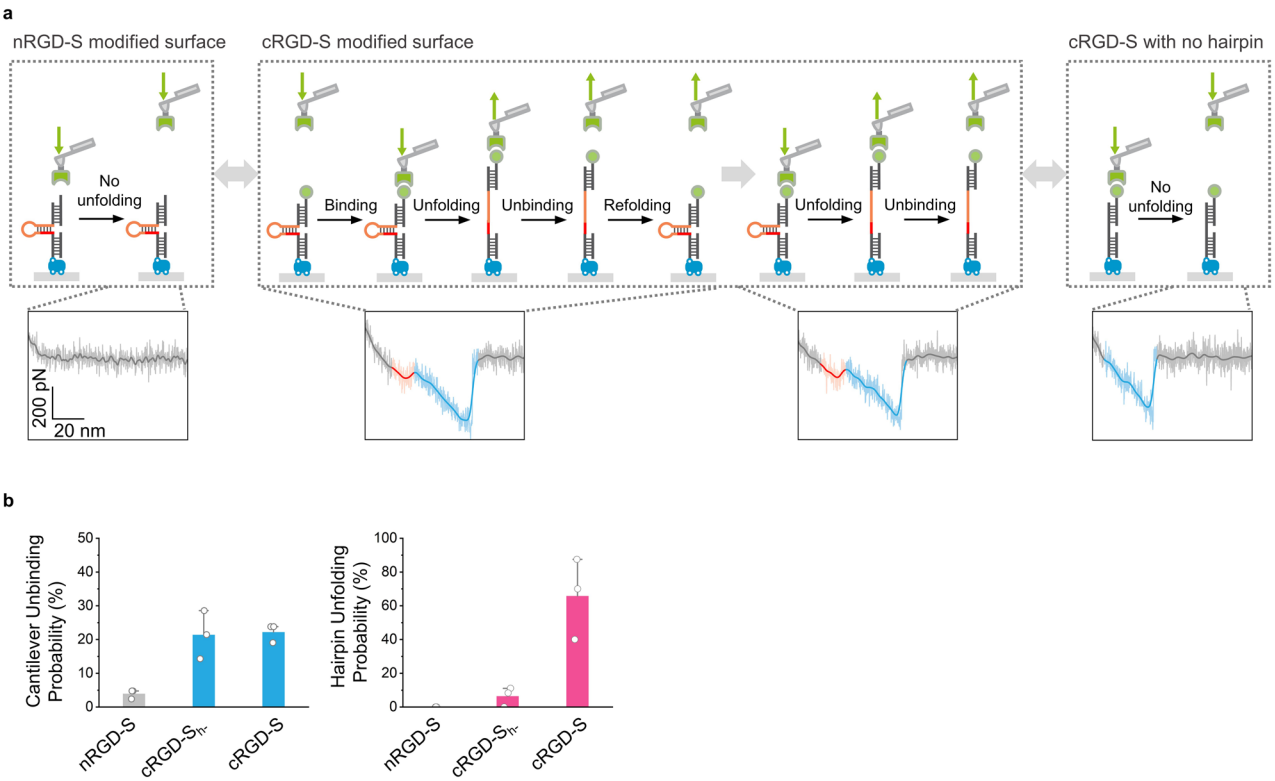

Extended Data Fig. 1 | Characterization of the mechanical fingerprint of the hairpin unfolding in the cRGD-S module using AFM. a, Typical force-extension (FE) curves between integrin-functionalized tip with surface modified with no cRGD conjugated S (nRGD-S), cRGD-S, and cRGD-S with absent hairpin structure (cRGD-S_{h^-}), respectively. For multiple pulling experiments, the hairpin was allowed to refold after one pulling cycle for 5 min, followed by the next pulling cycle. *Red* and *blue* peaks represent hairpin unfolding and cantilever unbinding, respectively. **b**, *Left:* Quantitative analysis for cantilever unbinding probabilities, calculated as the number of curves with unbinding peaks (the *blue* peak in the FE curve) divided by the total number of FE curves. *Right*: Quantitative analysis for hairpin unfolding probabilities relative to FE curves with the specific unbinding peak, calculated as the number of curves with hairpin unfolding peaks (the *red* peak in the FE curve) divided by the total number of curves with cantilever unbinding peaks (the *blue* peak in the FE curve). Data were measured from 126 curves from 3 independent experiments and shown as mean ± S.D. ($n = 3$). According to the probability kinetics model of 2D reactions, it is usually necessary to maintain a lower cantilever unbinding probability to obtain reliable single-molecule interaction data. Therefore, 20-25% unbinding probability in this study allows for a high probability of over 80% for single-molecule interactions, ensuring effective experimental condition control.

https://doi.org/10.1038/s41589-024-01572-x

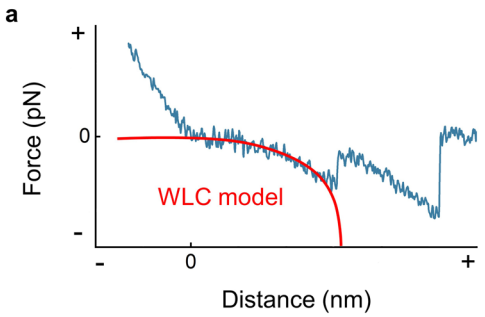

b

Hairpin	Persistence length L_p (nm)	ΔG (KJ/mol)
22%, 25 nt	1.06±0.33	40.06
77%, 25 nt	0.63±0.14	81.80
100%, 28 nt	0.38±0.06	149.67

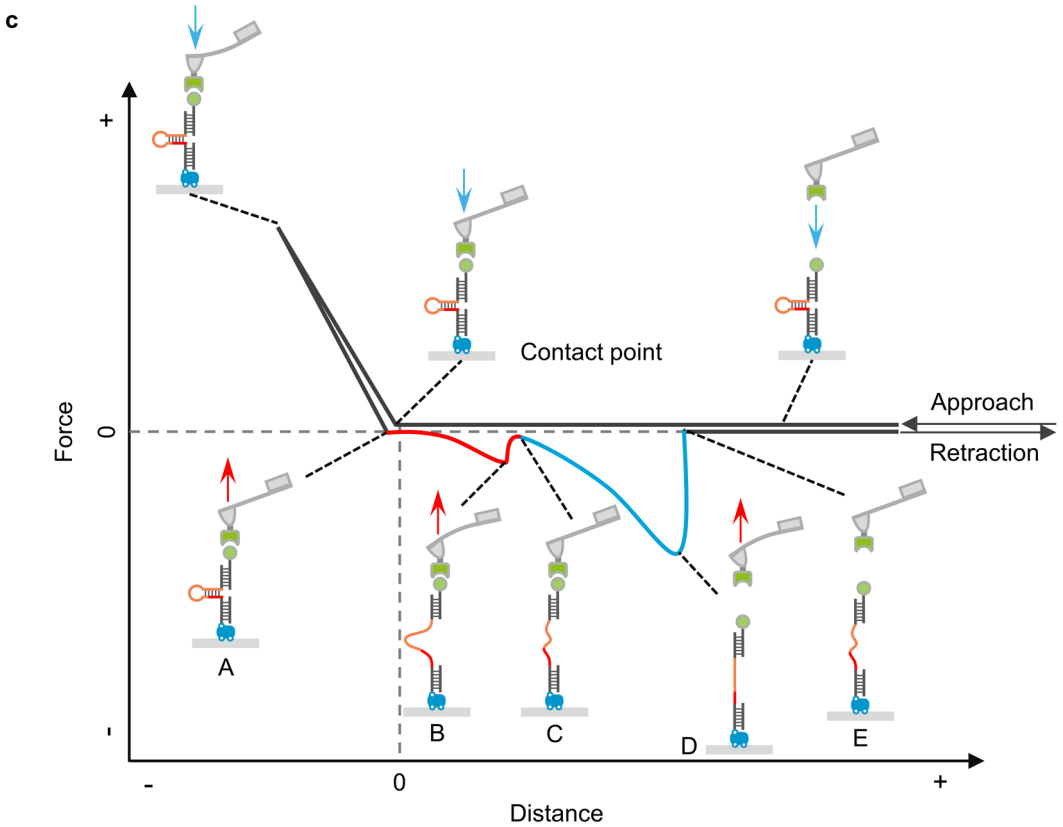

Extended Data Fig. 2 | Worm-like chain (WLC) model analysis. a, A typical FE curve (*blue*) and its theoretical fitting curve (*red*) based on the WLC model (The details please see Supplementary Note 3 in the supplementary information). **b**, Table of the values of the fitted persistence length L_p and calculated total free energy (ΔG). The persistence length L_p was fitted using WLC model from 60 curves from 3 independent experiments and presented as mean ± S.D. **c**, Schematic illustration of the approach-retraction process, delineating the reaction state at each stage. Within one approach and retraction cycle, the cantilever tip contacts the substrate-attached molecule cRGD-S, advancing into a repulsive contact regime until a compression force of 500 pN is reached. This phase is succeeded by the retraction of the tip. As retraction begins, the force initially reduces to a zero point, marking the start of the red hairpin unfolding region (Point A). As the distance between the substrate and cantilever increases, the S hairpin elongates, and the resulting decrease in its entropy generates a restoring force that bends the cantilever, depicted by the first small peak (Point B). Upon the unfolding of the hairpin domain, the DNA's contour length extends, bringing the force on the cantilever back to a near zero point. This juncture is noted as both the end of the red hairpin unfolding region and the start of the blue cantilever unbinding region (Point C). The further extension applies force on the cantilever again until the detachment of the unfolded S molecule from the AFM tip takes place, indicated by the second peak (Point D). Eventually, the force on the cantilever returns to a near zero point, marking the end of the blue cantilever unbinding region (Point E).

https://doi.org/10.1038/s41589-024-01572-x

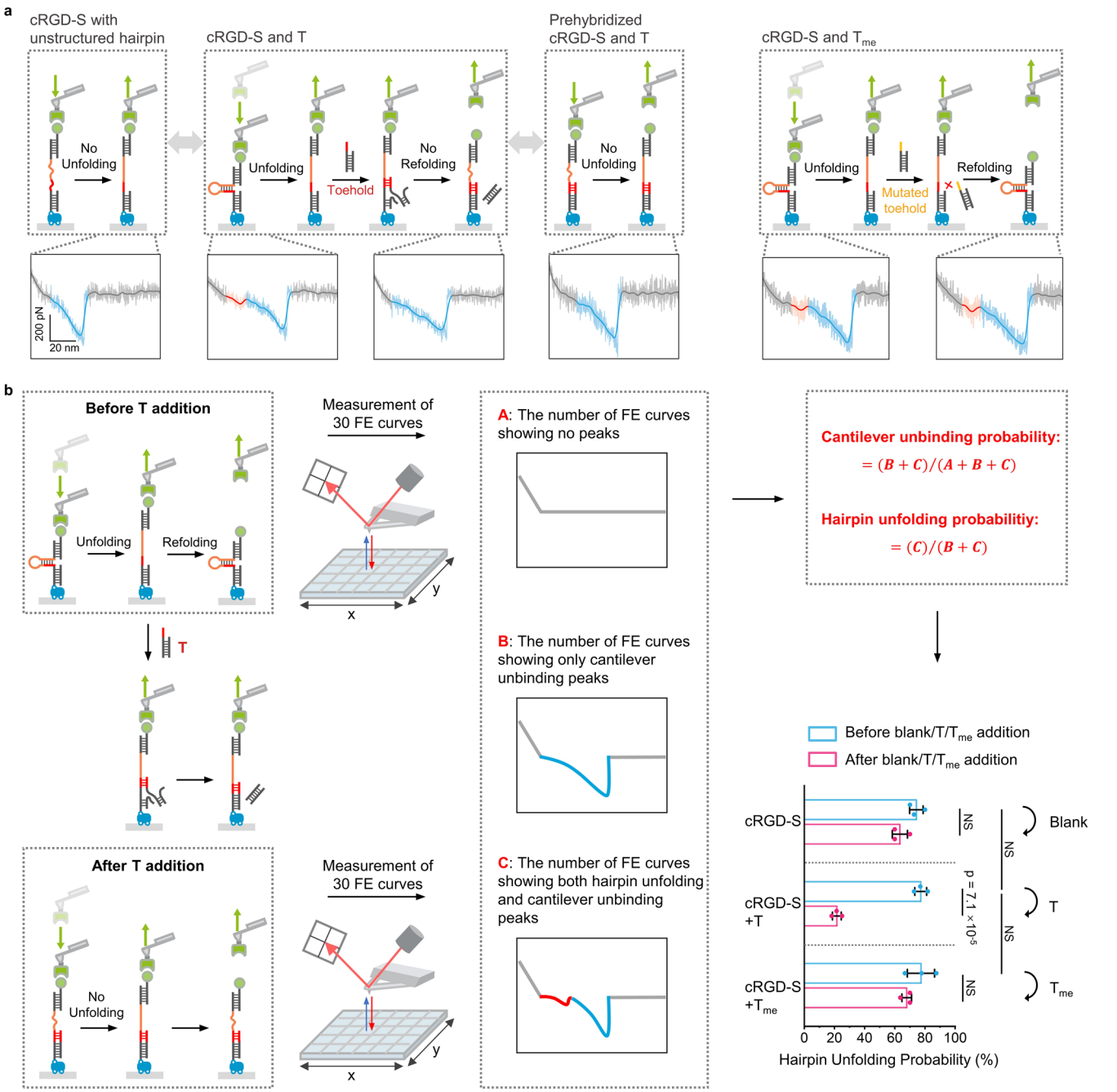

Extended Data Fig. 3 | Characterization of F-TSDR by AFM. a, Typical FE curves between the integrin-functionalized tip and cRGD-S modified surface in the presence of excess soluble free T modules or the control T modules with T_{me}. The contact between the integrin-functionalized tip and Sf/Sh/Te triplex-modified surface, the expected product of F-TSDR, was set as a positive control event. **b**, Schematic illustration of the experimental testing, data collection and probability calculation processes. Quantitative analysis for hairpin unfolding probabilities relative to FE curves with the specific unbinding peak, calculated as the number of curves with hairpin unfolding peaks (the *red* peak in the FE curve) divided by the total number of curves with cantilever unbinding peaks (the *blue* peak in the FE curve). *Blue* bars represent the hairpin unfolding probabilities for the cRGD-S-modified surface. *Fuchsia* bars represent the hairpin unfolding probabilities of the cRGD-S-modified surface in the presence or absence of T and T_{me} modules. Data were measured from 30 curves from 3 independent experiments. Data represent mean ± S.D. ($n = 3$), and significance was determined by unpaired two-tailed Student's *t*-test (*NS*, not significant). Before indicated treatments, the probability of hairpin unfolding among the three groups only varies within the range of 70% to 90%. This small variation in the hairpin unfolding probability can be attributed to the two factors, the inherently uncertainties associated with AFM as a single-molecule detection technique and potential system errors. The calculations through *t*-test show no statistically significant differences among the three groups as well as the samples before and after blank/T_{me} addition, whereas, after the addition of T, the probability of hairpin unfolding dramatically drops to ~20%. This significant difference sufficiently demonstrates the marked change in the probability of the hairpin unfolding after T addition, validating that the product of F-TSDR, Sf/Sh/Te triplex, prevents the unfolded hairpin from refolding.

https://doi.org/10.1038/s41589-024-01572-x

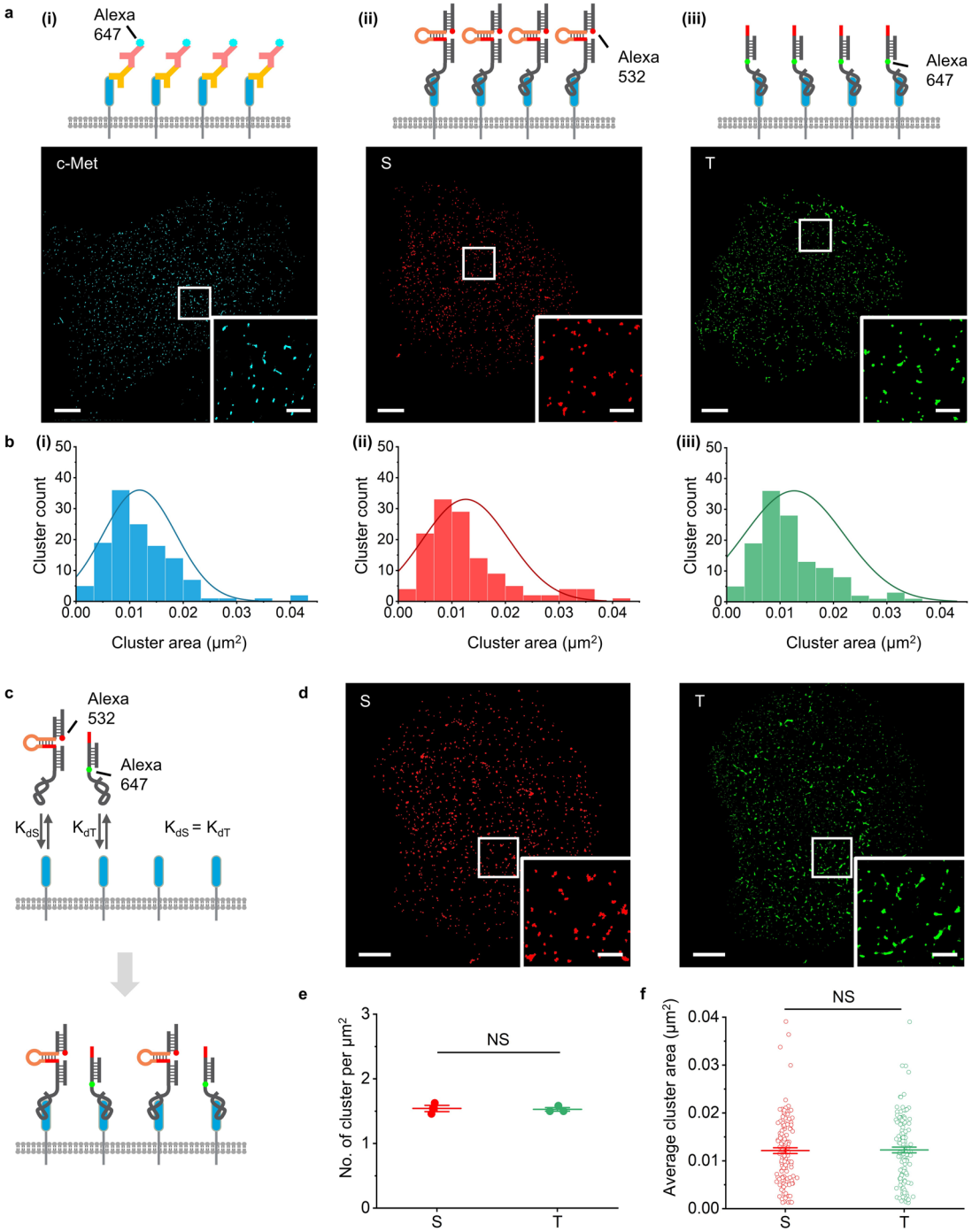

Extended Data Fig. 4 | Single colour dSTORM imaging of the cell surface distribution of c-Met, S, and T, respectively, and dual-colour dSTORM imaging for nanodomain analysis of S and T on a same cell. a, A549 cells were fixed and stained with different conditions: (i) with primary c-Met antibody followed by Alexa Fluor 647-labelled secondary antibody, (ii) with Alexa Fluor 532-labelled S, and (iii) with Alexa Fluor 647-labelled T. Scale bars represent 5 μm in the primary images and 1 μm in the zoomed-in images. **b**, The histogram showcases the frequency distribution of the different nanodomain sizes. Data is derived from 130 random nanodomains across 3 cells in three independent experiments. **c**, Schematic illustration of the dual-colour dSTORM imaging to visualize the nanodomains in the same cell labelled by S and T, both having comparable dissociation constants (shown in Supplementary Fig. 13 and 14). **d**, A549 cells underwent staining using Alexa Fluor 532-labelled S and Alexa Fluor 647-labelled T and subsequent fixation. The reconstructed dSTORM images for both Alexa Fluor 532-labelled S and Alexa Fluor 647-labelled T in a representative single cell were displayed. Scale bars indicate 5 μm in the original images and 1 μm in the magnified images. **e**, The graph depicts the average number of nanodomains per μm². **f**, The graph depicts the typical nanodomain areas. The data in **e** ($n = 3$) and **f** ($n = 130$) derive from 18 randomly chosen regions of interest (ROIs) with an area of 2×2 μm² from three cells in three independent experiments (a total of 130 nanodomains) and are presented as the mean ± S.D. There was no significant difference in the nanodomains of S and T captured in both channels, as determined by an unpaired two-tailed Student's *t*-test (*NS*, not significant).

https://doi.org/10.1038/s41589-024-01572-x

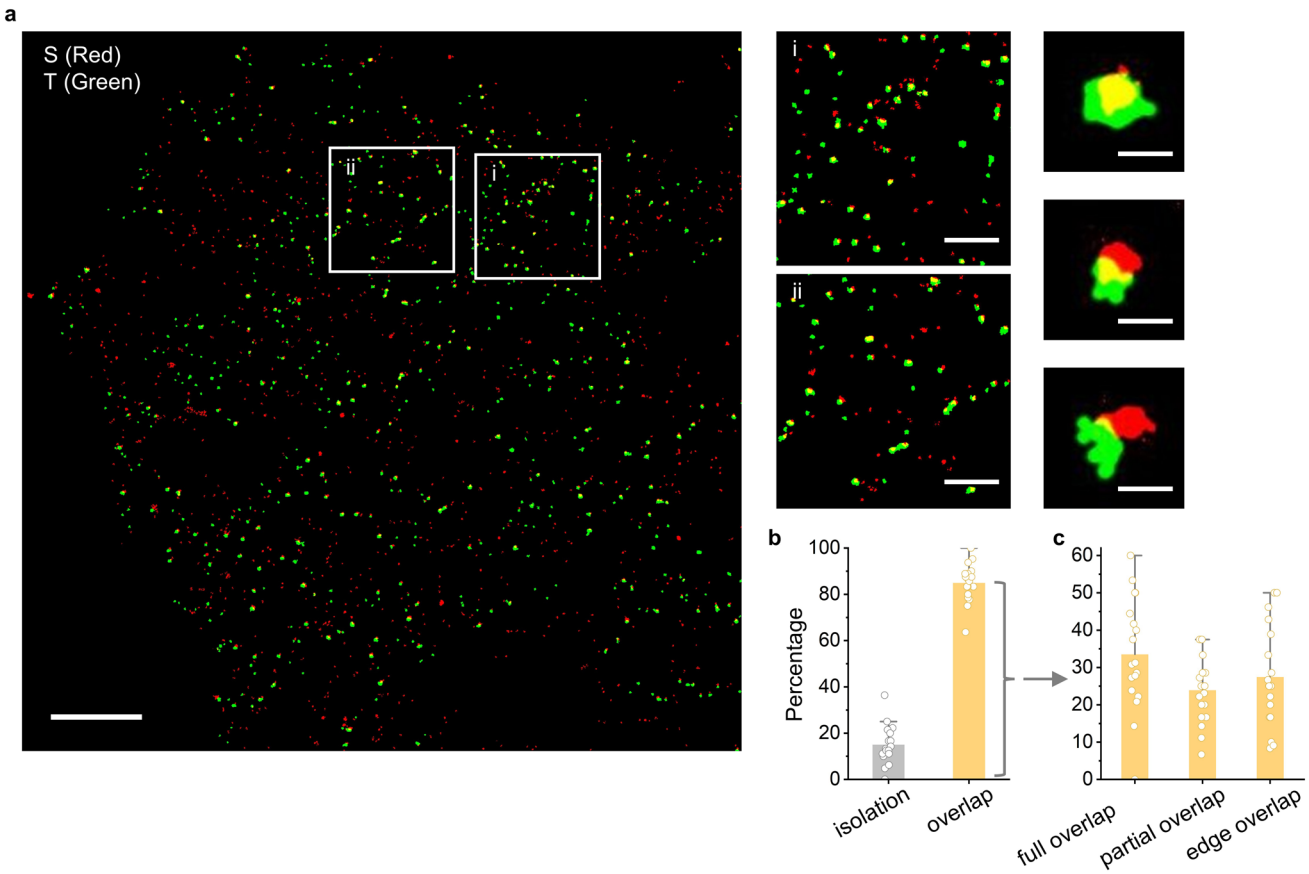

Extended Data Fig. 5 | Co-localization analysis of S and T using Dual-Colour dSTORM Imaging. a, A representative merged dual-colour dSTORM image showing the distribution of Alexa Fluor 532-labelled S and Alexa Fluor 647-labelled T on a single A549 cell. Two specific ROIs measuring 4 × 4 μm², labelled as (i) and (ii), are enlarged to highlight co-localization details. Further magnification illustrates three types of co-localization: full overlap, partial overlap, and edge overlap within individual nanodomains. The scale bars represent 5 μm for the main image, 1 μm for the enlarged ROIs, and 200 nm for the individual nanodomain images. **b**, For every dual-colour dSTORM image, 18 stochastically chosen ROIs of 3 × 3 μm² were extracted from three cells across three independent experiments (a total of 230 nanodomains) to analyse the spatial association between S and T positive nanodomains. The graph displays the co-localization relationships, presenting the percentages of isolated versus the overlapped nanodomains, with the overlaps categorized as full overlap, partial overlap and edge overlap. Data are presented as mean ± S.D. ($n = 18$). **c**, Further proportionate analysis of the overlapped nanodomains reveals the distribution among the three aforementioned overlap scenarios: full, partial, and edge overlap. These proportions are presented as mean ± S.D. ($n = 18$). According to the dual-colour dSTORM analysis, around 84% of the nanodomains (with diameters ranging 50 nm to 200 nm) showed overlap. Within these overlapped nanodomains of S-positive and T-positive signals, about 33% showed full overlap, 24% had partial overlap, and 27% demonstrated edge overlap. This analysis implies that on the entire membrane of a cell, 33% of S and T are colocalized and 51% of S and T are adjacent within the nanodomains. The details please see Supplementary Note 2 in the supplementary information.

https://doi.org/10.1038/s41589-024-01572-x

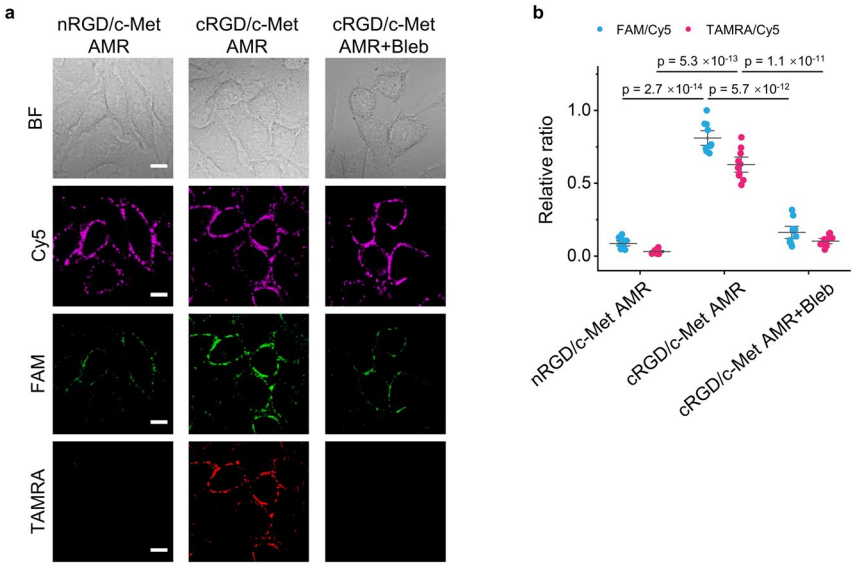

Extended Data Fig. 6 | Visualization of cRGD/c-Met AMR system upon sensing and transmitting integrin-mediated intercellular force on Hela cells. **a**, Representative images of brightfield, Cy5, FAM and TAMRA channels for the Hela cells treated with no cRGD conjugated AMR (nRGD/c-Met AMR) or cRGD/c-Met AMR (400 nM). For the actomyosin inhibition, Hela cells were pre-treated with Blebbistatin (10 μM) for 10 min before the addition of cRGD/c-Met AMR. Scale bar, 10 μm. **b**, Quantification of the relative FAM/Cy5 and TAMRA/Cy5 ratio to characterize the F-TSDR at cell-cell junctions. Data represent mean ± S.D. from independent experiments ($n = 10$). Significance was determined by unpaired two-tailed Student's t-test.

https://doi.org/10.1038/s41589-024-01572-x

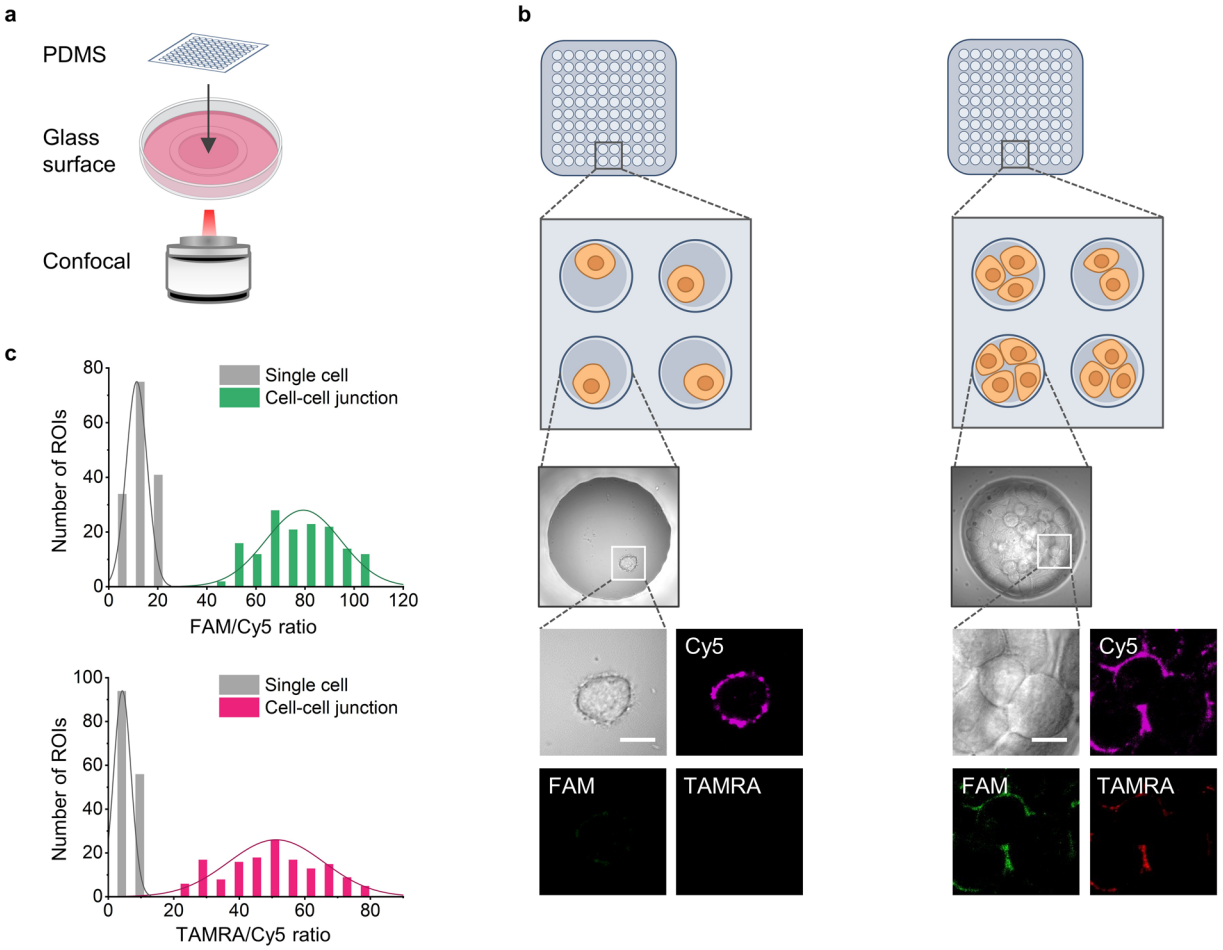

Extended Data Fig. 7 | The performance of AMR on isolated single-cell and multicell colony was examined using a high-density single-cell microarray. **a**, Schematic illustration of the fabrication of the microarray for visualization of GMD performance on isolated single-cell or multicell aggregation. The microarray was fabricated by attaching a PDMS stencil layer onto a flat glass surface of confocal dishes. **b**, Representative images of randomly chosen microwells with single-cell occupancy and multicell colony were presented. Successful AMR functionalization was visualized using Cy5 fluorescence as a reference signal. The force-sensing signal and force-transmitting signal are shown in FAM and TAMRA channels. Scale bars, 10 μm. **c**, To characterize the performance of the AMR, the force-sensing FAM/Cy5 ratios and force-transmitting TAMRA/Cy5 ratios were quantified from 150 regions of interest (ROIs) of 30 randomly chosen wells from three independent experiments. The graphs presented the frequency of occurrence of these ratios for isolated single cells and the cell-cell junctions in multi-colonies. A number of examples of the representative images of randomly chosen microwells with single-cell occupancy and multi-cell colony were presented in Supplementary Fig. 16. All of the isolated single cells exhibited obviously the reference Cy5 signals of AMR, indicating the successful functionalization of AMR on cell membrane, but neither force-sensing (FAM) nor transmitting (TAMRA) signals. In contrast, multi-cellular colonies manifested distinct FAM and TAMRA signals of AMR at cell-cell contacts. This data indicates that the operation of AMRs is fundamentally dependent on the forces exerted by the integrin receptors of adjacent cells, thereby highlighting the functionality of AMR in *trans* intercellular integrin-mediated mechanic interactions over *cis* integrin engagements within individual cells.

https://doi.org/10.1038/s41589-024-01572-x

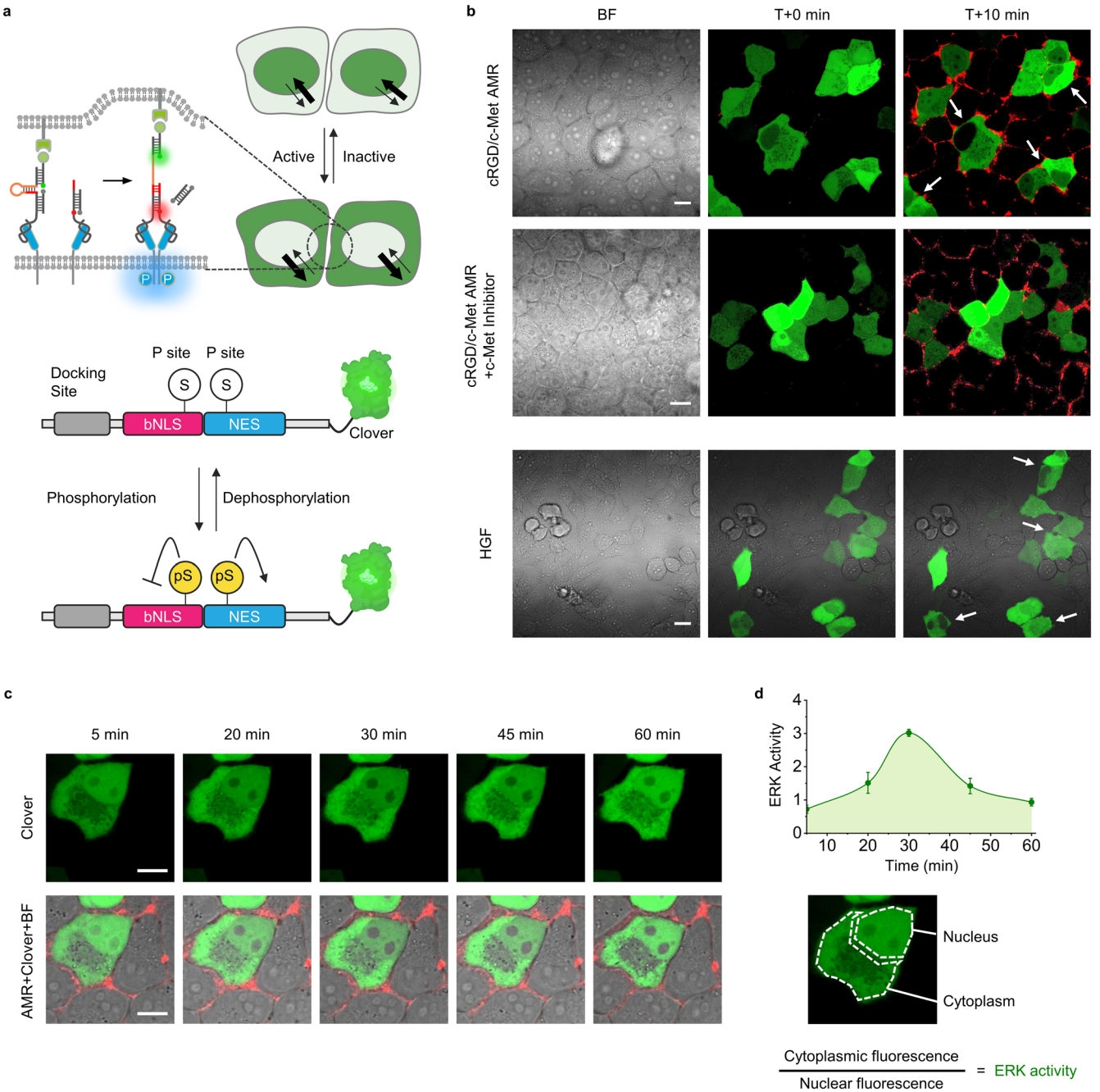

Extended Data Fig. 8 | Visualization of F-TSDR and ERK response activity of living cells. a, Schematic illustration of the ERK-KTR fused with the Clover protein. The ERK-KTRs are composed of an engineered construct in which a kinase substrate is fused to a bipartite nuclear localization signal (bNLS) and nuclear export signal (NES). The phosphorylation of the substrate suppresses bNLS activity and enhances NES activity, leading to cytoplasmic translocation. The shutdown of cell signalling pathways leads to the dephosphorylation of the substrate, which deactivates NES activity and recovers bNLS activity, leading to nuclear translocation. **b**, Hela cells were transfected with ERK-KTR for 24 h, followed by treatment of cRGD/c-Met AMR (400 nM) or HGF (2 nM). Cells were pre-treated with 100 nM Foretinib for 2 h to inhibit the kinase activity of c-Met. Time-lapsed images were collected to track the ERK-KTR translocation and TAMRA fluorescence change. The arrows indicate the cells experiencing nucleus-to-cytosol translocation of ERK-KTR. Scale bar, 10 μm. **c**, Sequential imaging captured from cRGD/c-Met AMR-modified HeLa cells post-transfection with ERK-KTR plasmids. Displayed images from the brightfield, Clover, and TAMRA fluorescence channels are colour-coded in *gray*, *green*, and *red*, respectively. Scale bars, 10 μm. **d**, Normalized ratio of the fluorescence intensities of ERK-KTR-Clover in the cytosol and nucleus are shown. Data represent mean ± S.D. ($n = 3$ from three independent experiments). The calculation of the ERK response ratio is calculated by dividing the number of cells with positive ERK translocation by the number of cells with Clover-positive. Noteworthy, nearly all of the cell with Clover-positive are accompanied by AMR activation signal, which illustrated the correlation between force-induced AMR activation at cell-cell junctions and the ERK activation. The translocation of the ERK reporter to the cytosol commenced and peaked at approximately 30 minutes. Following this peak, a gradual decline in cytosolic translocation was observed, which returned to baseline levels at around 60 minutes.

https://doi.org/10.1038/s41589-024-01572-x

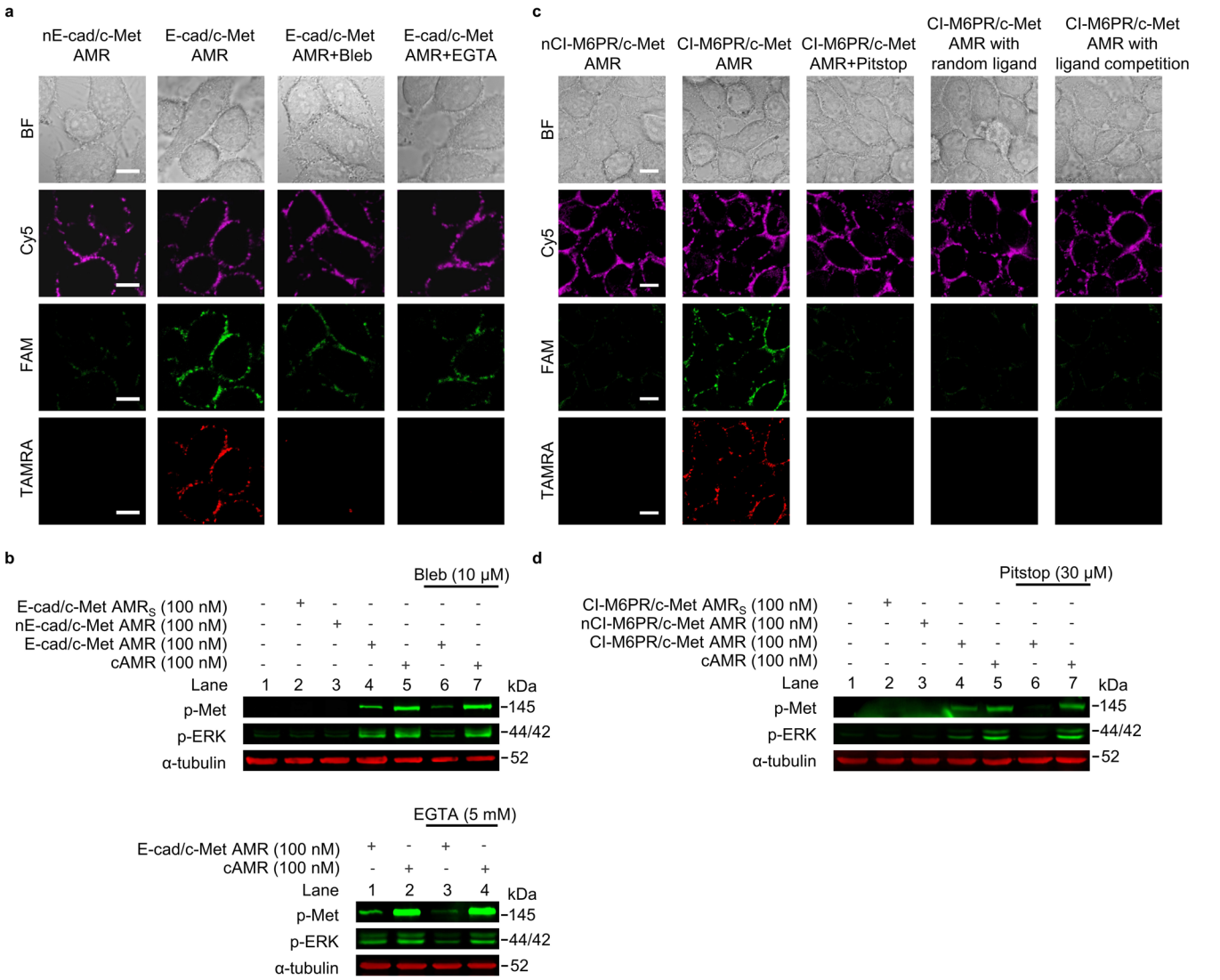

Extended Data Fig. 9 | Customized AMR with responsiveness to the E-cadherin-mediated force input and CI-M6PR endocytosis force input, respectively. a, Representative images for the nE-cad/c-Met AMR or E-cad/c-Met AMR-grafted A549 cells treated with or without Blebbistatin (10 μM) or EGTA (5 mM) are shown in the brightfield, Cy5, FAM, and TAMRA channels. Scale bars, 10 μm. **b**, Western blotting showed the c-Met phosphorylation (Tyr1234/Tyr1235) and ERK phosphorylation (Thr202/Tyr204) in the lysates of A549 cells with indicated treatments. The α-tubulin was used as an internal reference. E-cad/c-Met AMR_S represent the control in the absence of AMR-T. **c**, Representative images for the Hela cells engineered with 400 nM nCI-M6PR/c-Met AMR, CI-M6PR/c-Met AMR with random ligand sequence, and CI-M6PR/c-Met AMR, respectively, are shown in brightfield, Cy5, FAM and TAMRA channels. For the endocytosis inhibition, cells were pre-treated with Pitstop (30 μM) for 30 min before CI-M6PR/c-Met AMR functionalization. For the ligand competition control, cells were pre-treated with CI-M6PR aptamers (1 μM) for 30 min before CI-M6PR/c-Met AMR functionalization. Scale bar, 10 μm. **d**, Western blotting showed the c-Met phosphorylation (Tyr1234/Tyr1235) and ERK phosphorylation (Thr202/Tyr204) in the lysates of Hela cells with indicated treatments. The α-tubulin was used as an internal reference. CI-M6PR/c-Met AMR_S represent the control in the absence of AMR-T.

https://doi.org/10.1038/s41589-024-01572-x

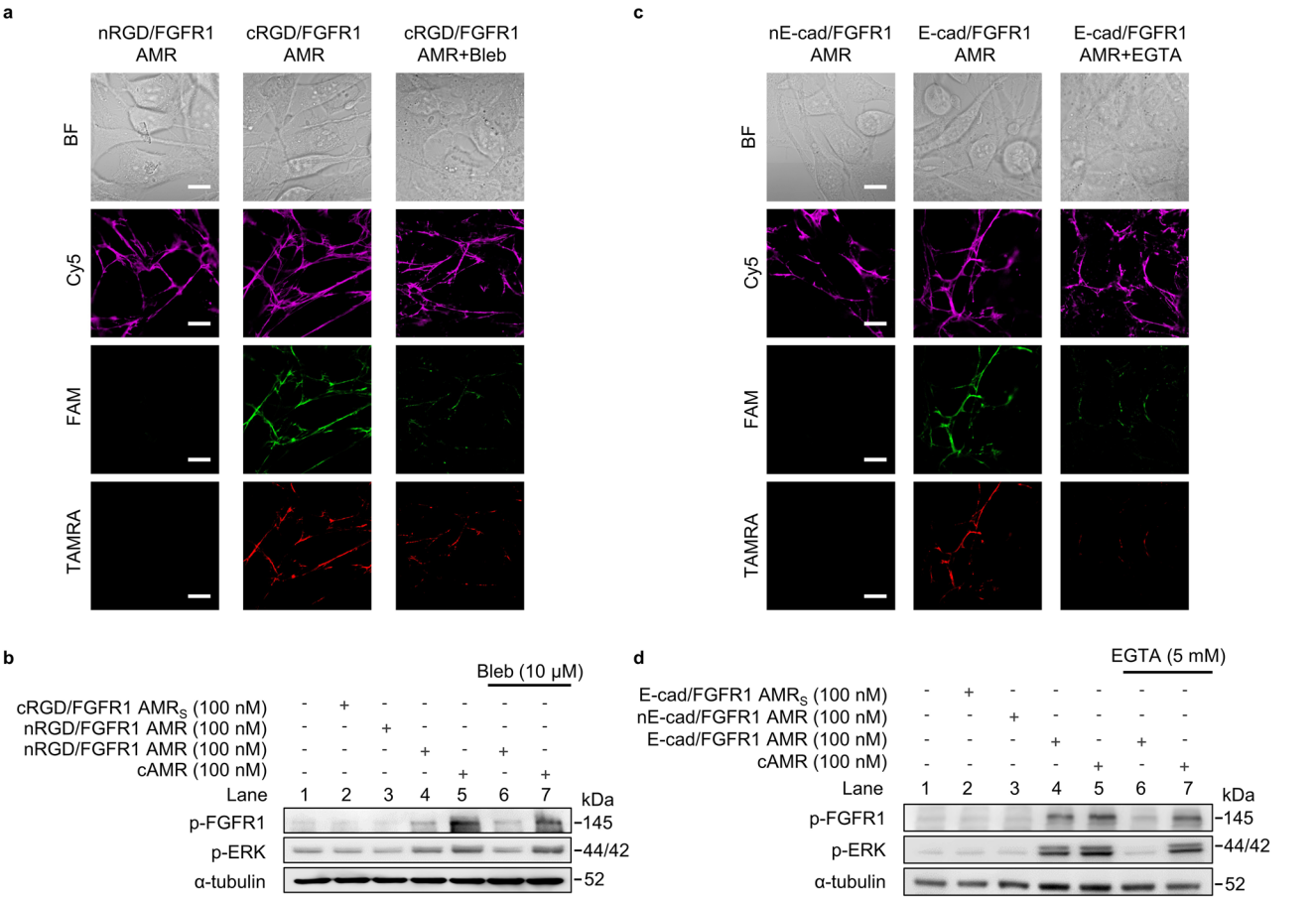

Extended Data Fig. 10 | The versatility of AMR to rewire integrin-mediated force input to promote FGFR1 signalling, and E-cadherin-mediated force input to promote FGFR1 signalling in neural stem cell maintenance, respectively. a, Representative images for the NIH3T3 cells engineered with 400 nM nRGD/FGFR1 AMR or cRGD/FGFR1 AMR are shown in brightfield, Cy5, FAM and TAMRA channels. For actomyosin inhibition, cells were pre-treated with Blebbistatin (10 μM) for 10 min before cRGD/FGFR1 AMR functionalization. Scale bar, 10 μm. **b**, Western blotting of FGFR1 phosphorylation (Tyr653/Tyr654) and ERK phosphorylation (Thr202/Tyr204) in the cell lysates of NIH3T3 cells with indicated treatments. The α-tubulin was used as an internal reference. cRGD/FGFR1 AMR_S represent the control in the absence of AMR-T. **c**, Neural stem cells (NSCs) were functionalized with nE-cad/FGFR1 AMR and E-cad/FGFR1 AMR at a concentration of 400 nM for 30 min. For the E-cadherin inhibition assay, cells were pre-treated with 5 mM EGTA for 30 min before E-cad/FGFR1 AMR functionalization. Following the incubation, cells were visualized using CLSM and representative images captured from brightfield, Cy5, FAM, and TAMRA channels are presented. Scale bar, 10 μm. **d**, Western blotting of FGFR1 phosphorylation (Tyr653/Tyr654) and ERK phosphorylation (Thr202/Tyr204) in the cell lysates of NSCs with indicated treatments. The α-tubulin was used as an internal reference. E-cad/FGFR1 AMR_S represent the control in the absence of AMR-T.

nature portfolio

Corresponding author(s): Zhou Nie

Last updated by author(s): Jan 22, 2024

Reporting Summary

Nature Portfolio wishes to improve the reproducibility of the work that we publish. This form provides structure for consistency and transparency in reporting. For further information on Nature Portfolio policies, see our Editorial Policies and the Editorial Policy Checklist.

Statistics

For all statistical analyses, confirm that the following items are present in the figure legend, table legend, main text, or Methods section.

n/a	Confirmed
☐	☒ The exact sample size (*n*) for each experimental group/condition, given as a discrete number and unit of measurement
☐	☒ A statement on whether measurements were taken from distinct samples or whether the same sample was measured repeatedly
☐	☒ The statistical test(s) used AND whether they are one- or two-sided *Only common tests should be described solely by name; describe more complex techniques in the Methods section.*
☒	☐ A description of all covariates tested
☒	☐ A description of any assumptions or corrections, such as tests of normality and adjustment for multiple comparisons
☐	☒ A full description of the statistical parameters including central tendency (e.g. means) or other basic estimates (e.g. regression coefficient) AND variation (e.g. standard deviation) or associated estimates of uncertainty (e.g. confidence intervals)
☐	☒ For null hypothesis testing, the test statistic (e.g. *F*, *t*, *r*) with confidence intervals, effect sizes, degrees of freedom and *P* value noted *Give P values as exact values whenever suitable.*
☒	☐ For Bayesian analysis, information on the choice of priors and Markov chain Monte Carlo settings
☒	☐ For hierarchical and complex designs, identification of the appropriate level for tests and full reporting of outcomes
☒	☐ Estimates of effect sizes (e.g. Cohen's *d*, Pearson's *r*), indicating how they were calculated

Our web collection on statistics for biologists contains articles on many of the points above.

Software and code

Policy information about availability of computer code

Data collection	1. TIRF images were acquired using LAS X v3.7.23463.4 (Leica), confocal images were acquired using NIS-Elements v4.60.00 (Nikon), and dSTORM images were acquired using NEO software v2 (Abbelight). 2. AFM force spectroscopy and images were obtained using JPK BioAFM software v7 (Bruker) and ZEN v2.3.69 (Zeiss). 3. Western blots were performed using Image Studio software v3.1.4 (LI-COR) and Azure Imaging Systems v2.1.0 (Bio-Rad). 4. qPCR results were recorded with QuantStudio Real-Time PCR Software v1.7.1 (Applied Biosystems). 5. Flow cytometry data were collected using CytExpert software v2.4.0 (Beckman). 6. The gels images were acquired by Azure Imaging Systems v2.1.0 (Bio-Rad). 7. The SPR data were collected using Biacore 8K Control Software v3.0.12. 8. The images of neural stem cells were acquired by Gen5 v3.05 (BioTek).
Data analysis	1. Microscopic and gel images were analyzed by ImageJ v2.9.0. 2. The AFM data were analyzed by JPKSPM Data Processing v2.7.10. 3. The flow cytometry results were analyzed using FlowJo v10. 4. The SPR results were analyzed using Biacore Insight Evaluation Software v3.0.12. 5. Data processing and statistical analysis were performed by Microsoft Excel v16.0 and Origin v10.0.5.

For manuscripts utilizing custom algorithms or software that are central to the research but not yet described in published literature, software must be made available to editors and reviewers. We strongly encourage code deposition in a community repository (e.g. GitHub). See the Nature Portfolio guidelines for submitting code & software for further information.

Data

Policy information about availability of data

All manuscripts must include a data availability statement. This statement should provide the following information, where applicable:

- Accession codes, unique identifiers, or web links for publicly available datasets
- A description of any restrictions on data availability
- For clinical datasets or third party data, please ensure that the statement adheres to our policy

All data supporting the findings of this study are available within the article and its Supplementary Information. Source data are provided in this manuscript.

Human research participants

Policy information about studies involving human research participants and Sex and Gender in Research.

Reporting on sex and gender	N/A
Population characteristics	N/A
Recruitment	N/A
Ethics oversight	N/A

Note that full information on the approval of the study protocol must also be provided in the manuscript.

Field-specific reporting

Please select the one below that is the best fit for your research. If you are not sure, read the appropriate sections before making your selection.

☒ Life sciences ☐ Behavioural & social sciences ☐ Ecological, evolutionary & environmental sciences

For a reference copy of the document with all sections, see nature.com/documents/nr-reporting-summary-flat.pdf

Life sciences study design

All studies must disclose on these points even when the disclosure is negative.

Sample size	No sample size calculation was performed. All experiments were carried out in at least three replicates, which was sufficient for consistent and reproducible results to support this paper. The exact sample size of each experiment was given in the corresponding figure legend.
Data exclusions	No data were excluded from the analysis.
Replication	At least three or more replicates were performed. All attempts at replication were successful.
Randomization	Randomization was not relevant for this study because both control and experimental samples were treated in the same culturing environment and experiments were performed following the same protocols.
Blinding	Blinding was not necessary for this study since our data analyses are based on objectively measurable data, which are not subject to human bias.

Reporting for specific materials, systems and methods

We require information from authors about some types of materials, experimental systems and methods used in many studies. Here, indicate whether each material, system or method listed is relevant to your study. If you are not sure if a list item applies to your research, read the appropriate section before selecting a response.

Materials & experimental systems

n/a	Involved in the study
☐	☒ Antibodies
☐	☒ Eukaryotic cell lines
☒	☐ Palaeontology and archaeology
☒	☐ Animals and other organisms
☒	☐ Clinical data
☒	☐ Dual use research of concern

Methods

n/a	Involved in the study
☒	☐ ChIP-seq
☐	☒ Flow cytometry
☒	☐ MRI-based neuroimaging

Antibodies

Antibodies used

Anti-Met Rabbit mAb (1:1000 and 1:1500), Cell Signalling Technology, #8198
Anti-Phospho-Met (Tyr1234/1235) Rabbit mAb (1:1000), Cell Signalling Technology, #3077
Anti-Integrin β3 Rabbit mAb (1:1000), Cell Signalling Technology, #13166
Anti-Phospho-FGF Receptor 1 (Tyr653/654) Rabbit mAb (1:1000), Cell Signalling Technology, #52928
Anti-Phospho-p44/42 MAPK (Erk1/2) (Thr202/Tyr204) Rabbit mAb (1:2500), Cell Signalling Technology, #4370
Anti-CDH1 rabbit polyclonal antibody (1:1000), Sangon Biotech, #D260656
Anti-α-tubulin monoclonal antibody [DM1A] (1:2500), Cellway Biotechnology, #18073008-1
IRDye 680RD goat anti-mouse secondary antibody (1:10000), LI-COR, #925-68070
IRDye 680RD goat anti-rabbit secondary antibody (1:10000), LI-COR, #925-68071
HRP-conjugated goat anti-rabbit secondary antibody (1:2500), Thermo Fisher Scientific, #31460
HRP-conjugated goat anti-mouse secondary antibody (1:2500), Thermo Fisher Scientific, #31430
Nestin Rabbit Monoclonal Antibody [SP103] (1:200), Beyotime, #AF2215
Alexa Fluor 488-labeled Goat Anti-Rabbit IgG secondary antibody (1:500), Beyotime, #A0423
Alexa Fluor 647-labeled Goat Anti-Rabbit IgG secondary antibody (1:25), Beyotime, #A0468

Validation

Anti-Met antibody validation (https://antibodyregistry.org/search.php?q=AB_10858224)
Anti-Phospho-Met antibody validation (https://antibodyregistry.org/search.php?q=AB_2143884)
Anti-Integrin β3 antibody validation (https://antibodyregistry.org/search.php?q=AB_2798136)
Anti-Phospho-FGF Receptor 1 antibody validation (https://antibodyregistry.org/search.php?q=AB_2799424)
Anti-Phospho-p44/42 MAPK antibody validation (https://antibodyregistry.org/search.php?q=AB_2315112)
Anti-CDH1 antibody validation (https://www.sangon.com/productDetail?productInfo.code=D260656)
Anti-α-tubulin antibody were validated by the manufacturer.
IRDye 680RD goat anti-mouse secondary antibody validation (https://www.antibodyregistry.org/AB_2651128)
IRDye 680RD goat anti-rabbit secondary antibody validation (https://www.antibodyregistry.org/AB_2721181)
HRP-conjugated goat anti-rabbit secondary antibody validation (https://www.antibodyregistry.org/AB_228341)
HRP-conjugated goat anti-mouse secondary antibody validation (https://www.antibodyregistry.org/AB_228307)
Nestin Rabbit Monoclonal Antibody validation (https://www.beyotime.com/product/AF2215.htm)
Alexa Fluor 488-labeled Goat Anti-Rabbit IgG secondary antibody validation (https://www.beyotime.com/product/A0423.htm)
Alexa Fluor 647-labeled Goat Anti-Rabbit IgG secondary antibody validation (https://www.beyotime.com/product/A0468.htm)

Eukaryotic cell lines

Policy information about cell lines and Sex and Gender in Research

Cell line source(s)	Hela (human cervical carcinoma cell line), A549 (human lung carcinoma cell line) and NIH3T3 (mouse fibroblast cell line) cells were obtained from ATCC. NSC (human neural stem cell line) was obtained from the Cellway Biotechnology.
Authentication	The cell lines used were authenticated by the commercial source. No additional cell line authentication was performed.
Mycoplasma contamination	Cell lines tested negative for mycoplasma.
Commonly misidentified lines (See ICLAC register)	No commonly misidentified cell lines were used.

Flow Cytometry

Plots

Confirm that:

☒ The axis labels state the marker and fluorochrome used (e.g. CD4-FITC).

☒ The axis scales are clearly visible. Include numbers along axes only for bottom left plot of group (a 'group' is an analysis of identical markers).

☒ All plots are contour plots with outliers or pseudocolor plots.

☒ A numerical value for number of cells or percentage (with statistics) is provided.

Methodology

Sample preparation	Hela cell suspension were enzymatically lifted and incubated with Cy5-labelled samples in PBS for 20 min. After being washed with PBS, the cells were analysed by flow cytometry.
Instrument	CytoFLEX Flow Cytometer (Beckman)
Software	CytExpert software (Beckman)
Cell population abundance	At least 10,000 cells were used for other flow cytometry analysis and approximately 1000 events were filtered out upon gating.
Gating strategy	Cells were first gated based on FSC-A vs. SSC-A to exclude debris and non-viable cells. Cells incubated with control samples were used for selecting negative population. Cy5-labelled cells were then identified using a gate based on the negative control sample.

☒ Tick this box to confirm that a figure exemplifying the gating strategy is provided in the Supplementary Information.